PHYSICAL REVIEW D **67**, 073022 (2003)

Atmospheric muon and neutrino flux from 3-dimensional simulation

Yong Liu,* L. Derome,† and M. Buénerd‡
Institut des Sciences Nucléaires, 53 av. des Martyrs, 38026 Grenoble cedex, France

(Received 29 November 2002; published 29 April 2003)

The atmospheric muon and neutrino flux have been simulated using the same approach which successfully accounted for the recent secondary proton, electron, and positron flux measurements in orbit by the AMS experiment. For the muon flux, good agreement is obtained with the CAPRICE and HEAT data for altitudes ranging from sea level up to about 38 km. The general features of the calculated atmospheric neutrino flux are reported and discussed. The flux obtained at the Super-Kamiokande experiment location are reported and compared with other calculations. For low neutrino energies the flux obtained is significantly smaller than that used in the data analysis of underground experiment. The simulation results for the SOUDAN experiment site are also reported.

DOI: 10.1103/PhysRevD.67.073022 PACS number(s): 96.40.Tv, 14.60.Pq, 95.85.Ry

I. INTRODUCTION

With the rapidly increasing amount and statistical significance of the data collected by underground neutrino detectors [1,2], the precise calculation of the atmospheric neutrino flux is highly desirable, since the interpretation of the data relies on the calculated flux as a fundamental input. In the contained events analysis, the ratio of ratios—namely, the ratio of the observed number of muon events to the number of observed electron events with the corresponding ratio of the same numbers from simulation calculations—is not sensitive to the absolute neutrino flux. However, in the analysis of upward going muon events, the absolute flux need to be known accurately in addition to the detailed features of the flux such as the zenithal and azimuthal angle distribution [3,4]. The availability of calculations of proven validity would discard all possible doubt on the conclusions.

In the past 20 years, various methods including analytical, semianalytical [5,6], kinematical [7], and Monte Carlo techniques [8,9] have been applied to calculate the atmospheric neutrino flux [5,8–12]. However, the accuracy of the results was limited by the accuracy on both the cosmic ray (CR) abundance and the production cross section of the parent particle ($\pi^{\pm}, K^{\pm}, K_L^0, K_S^0$) in the collisions of CRs with atmospheric nuclei over the relevant energy range [13,14], used in these calculations, these two quantities being basic inputs to the calculations. The analysis and the comparisons made in [15] indicated that the particular choice of the primary spectra and the strong interaction model, as well as Earth's geomagnetic field could result in significant differences in the calculated neutrino flux.

The new AMS [16] and BESS [17] measurements of the CR proton flux consistently agree to within 5%. The values reported are lower than those used in the previous works by about 20%–25% [18]. In addition, some analyses [19] showed that the pion production cross sections given by the general purpose software based on theoretical models may largely depart from experimental data.

Although the values of the flavor ratio reported in previous works are very close to each other, the absolute values of the flux obtained in these works fail to be consistent with each other within satisfying precision [15]. In particular, these results seem not to predict quantitatively the observed east-west (EW) asymmetry of the neutrino induced events [20,21] which is expected to originate from the EW asymmetry of the geomagnetic cutoff (GC) on the incoming CR—mainly protons and helium particles here—momentum, due to Earth's magnetic field. Any calculation, to be reliable, must reproduce the experimental EW asymmetry since flavor oscillations do not change the direction of motion. This requirement can be taken as a testing ground for the various approaches of the neutrino flux calculations.

With the occurrence of the new measurements of the primary CR flux, together with the continuous improvement of the cross section calculations, most approaches have been updated [18,22–25], and new calculations have been proposed [26–30]. In parallel, experimental groups also made greater effort aiming at understanding the neutrino production process in the atmosphere [31–33] with the measurements on the muon flux at various altitudes, together with those of the primary proton and helium flux. These new data provided a sounder testing ground for the reliability of the numerical approaches to the particle production and to the particle dynamics and kinematics in the atmosphere and in Earth's geomagnetic field.

The work reported here is an extension of a research program which primary motivations were to interpret the AMS01 measurements of the charged particle flux in near Earth orbit [16,34]. To this purpose, an event generator describing the CR-induced cascade in the atmosphere, particle propagation in geomagnetic field, and interactions with the medium has been developed and successfully used to reproduce the proton [35], electron-positron [36], and helium 3 [37] flux data measured by AMS and their relevant dependence on the geomagnetic coordinates. Since the $e^{\pm}$ generator of the program was basically the same as needed to generate the muon and neutrino flux, the code could be rather straightforwardly extended to describe the latter and to ad-

---

*Present address: MS 309, FermiLab, P.O. Box 500, Batavia, IL 60510. Electronic address: yongliu@fnal.gov

†Electronic address: derome@isn.in2p3.fr

‡Corresponding author. Electronic address: buenerd@isn.in2p3.fr

©2003 The American Physical Society

dress the important issue of the atmospheric neutrino flux. It should be emphasized that the present approach allows an evaluation of the neutrino flux induced by both the primary CR flux and the atmospheric secondary flux, which have been tested sensitively and independently on other observables, conferring to the results a character of sound reliability. The above issues will be discussed in detail below. This approach is also being successfully applied to the calculation of the atmospheric secondary flux of antinucleons [38].

The article reports on the calculation of the atmospheric muon and neutrino flux. The paper is organized as follows. In Sec. II, the method and models used in the calculations are introduced. Section III is devoted to the results on the muon flux. In Sec. IV, the properties of the calculated neutrino flux averaged on the whole terrestrial sphere are discussed, while the properties of the local neutrino flux calculated at the location of the Super-Kamiokande detector are discussed in Sec. V. In the following Sec. VI the neutrino flux at the Soudan detector location is discussed along the same lines. Summary and conclusions are given in Sec. VII.

II. METHODS AND MODELS

The method of calculation and the models used in the simulation program are described in [35,36]. The calculation proceeds by means of a full 3D-simulation program. The main features of this approach are listed below for the reader's convenience, with emphasis on some particular points relevant to the neutrino and muon flux.

(1) CR generation: Incident cosmic rays are generated on a virtual sphere chosen at some distance from Earth as discussed below. Events are generated randomly and uniformly on this sphere. In order to get an isotropic flux at any point inside the volume of the virtual sphere, the differential element of the zenith angle distribution of the particle direction generated on the sphere must be proportional to $\cos\theta_z\, d(\cos\theta_z)$, θ_z being the zenithal angle of the particle [11,22] (see also [24]). The particle (A and Z) and its momentum are then generated according to the CR abundances and spectra discussed below. Generating random events on a virtual sphere far enough from Earth, i.e., at a distance where the geomagnetic field effects are negligible, so that the CR flux is isotropic, would imply a very large distance from Earth and thus the generation of a tremendous number of events, most of them being useless for the simulation purpose since they would not reach the Earth-atmosphere system. Instead of this time consuming direct method, the generation sphere is chosen close to Earth, at a 2000 km altitude. The geomagnetic cutoff is then applied by backtracing the particle trajectory in the geomagnetic field. In this procedure, only those particles reaching a backtracing distance of 10 Earth radii are kept in the sample. Flux conservation along any allowed particle path in the geomagnetic field is ensured by Liouville's theorem application [39].

(2) CR abundances: For the incident CR proton and helium flux, functional forms fitted to the 1998 AMS measurements were used [16,34]. For other periods of the solar cycle than those of the measurements, the incident cosmic flux is corrected for the different solar modulation effects using a simple force law approximation [40]. The main components of the incident CR flux are usually divided in the following most abundant groups of elements: p, He, CNO, Ne-S, and Fe. The contribution of each group to the neutrino flux scales roughly with the product $\phi(\langle z\rangle)\mu(\pi)$ with $\phi(\langle z\rangle)$ the CR abundance of the element or group of elements with mean electric charge $\langle z\rangle$, and $\mu(\pi)$ the average multiplicities of pions produced in the CR collisions with atmospheric nuclei. This is approximate since secondary protons induced by the He component also contributing to this production are not taken into account in this product. Table I shows the relative abundances of the estimated pion flux induced by the various components of the CR flux. They have been evaluated using the AMS measurements for p and He and those from [41] for the heavier elements with the spectral index from [42]. The flux has been calculated for particle rigidities above a geomagnetic cutoff of 10 GV. The pion multiplicities were taken from [43,44] at 4.2 GeV/c per nucleon. The sum of the contributions from the $A>4$ flux components amounts to about 6%, while it is 72% for p and 22% for He. This choice for the GC maximizes the He (and heavier elements) over the p fraction, which would be smaller for a lower cutoff (the He fraction would be around 10% for no cutoff). The $A>4$ components of the CR flux were not taken into account in the present calculations. They will be included in the further developments of the code.

(3) Particle propagation: Each particle is propagated in the geomagnetic field and interacts with nuclei of the local atmospheric density. The specific ionization energy loss is computed for each step along the trajectory. The model used to describe the atmospheric density was taken from Ref. [45]. Every secondary particle is processed the same way as its parent particle, leading to the generation of atmospheric cascades.

(4) Secondary particle production: Nucleons, pions, and kaons are produced with their respective cross sections. For these particles the Kalinovsky-Mokhov-Nikitin (KMN) parametrization of the inclusive cross sections [46] was used. For pions the KMN parameters have been fit on a wide range of $p+A\rightarrow\pi^{\pm,0}$ data between 1.38 and 400 GeV/c incident momenta [19,47]. Leptons—electrons, muons, and neutrinos—are produced in the decay chains of mesons, mainly pions and kaons, hadronically produced on atmospheric nuclei A in processes of type: $CR+A\rightarrow M+X$, $M\rightarrow\mu+\nu$, $\mu\rightarrow e+\nu+\bar{\nu}$. See below for details. It must be emphasized here that the constraint to reproduce simultaneously the lepton population measurements at various altitudes and geographical coordinates is extremely strong and that a successful result would ensure a high level of reliability of the theoretical grounds and of the numerical approach to the problem.

(5) μ decay: For the decay of muons, the spectra of the products $(\nu,\bar{\nu},e^{\pm})$ are generated according to the Fermi theory.

(6) K decay: For kaon decay, the Dalitz plot distribution given in [48] is used.

(7) μ polarization effects: Muon polarization was taken

TABLE I. Mean flux $\phi(z)(\mathrm{m}^2\cdot\mathrm{s}\cdot\mathrm{sr})^{-1}$, π^- multiplicity $\langle\mu(\pi)\rangle$, of the components of the CR flux, and their product normalized to 1, for the conditions described in the text.

Particle type	p	He	CNO	Ne-S	Fe
$\langle\phi(\langle z\rangle)\rangle$	106	16	1.1	0.34	0.08
$\langle\mu(\pi^-)\rangle$	0.3	0.63	1.23	1.53	1.86
Fractional π^- flux	0.72	0.22	0.032	0.011	0.0035

into account for pion decay and for the $K^\pm\rightarrow\mu^\pm\nu_\mu(\overline{\nu_\mu})$ channel [9,11,49].

(8) CR energy range: The kinetic energy range of incident CRs covered in the simulation is [0.2,2000] GeV, from around the pion production threshold up to a value where the corresponding neutrino flux produced becomes negligible.

(9) Processing: Each particle history, trajectory parameters, and kinematics are traced and recorded by the program. The event file was then analyzed separately to generate the various distributions of interest.

(10) ν detection: For the neutrino flux calculation, a virtual detection sphere is defined at the Super-Kamiokande detector altitude.

(11) Flux normalization: The differential particle flux produced in the simulation $(\mathrm{m}^{-2}\cdot\mathrm{s}^{-1}\cdot\mathrm{sr}^{-1}\cdot\mathrm{GeV}^{-1})$ were calculated by dividing the number of particles detected by the (local) surface of the particle collection area, solid angle, energy bin size, and equivalent sampling time of the CR flux. The latter was obtained from the total event number generated in the simulation run(s) divided by the surface of the generation sphere times the integrated ($\cos\theta_z$ weighted) solid angle π) times the energy integrated flux.

To increase the statistics for the energy regions of low particle flux, the primary spectra were separated into a set of energy intervals such as [0.2,50],[50,100], . . . , [450,500], [500,600], . . . , [900,1000], [1000,1250], . . . , [1750,2000] GeV; the simulation program was run separately for each primary energy bin and appropriately renormalized later when the full sample was constituted. The corresponding exposure times ranged from 2.1×10^{-12} s for the lowest energy bin to 4.7×10^{-10} s for the highest energy bin, corresponding to a total of the order of 10^8 events generated in the sample.

These calculations as those reported previously [35–37] include no adjustable parameter.

III. ATMOSPHERIC MUON SPECTRA

As was mentioned above, atmospheric muons are produced in the decay chain of pions and kaons produced in the

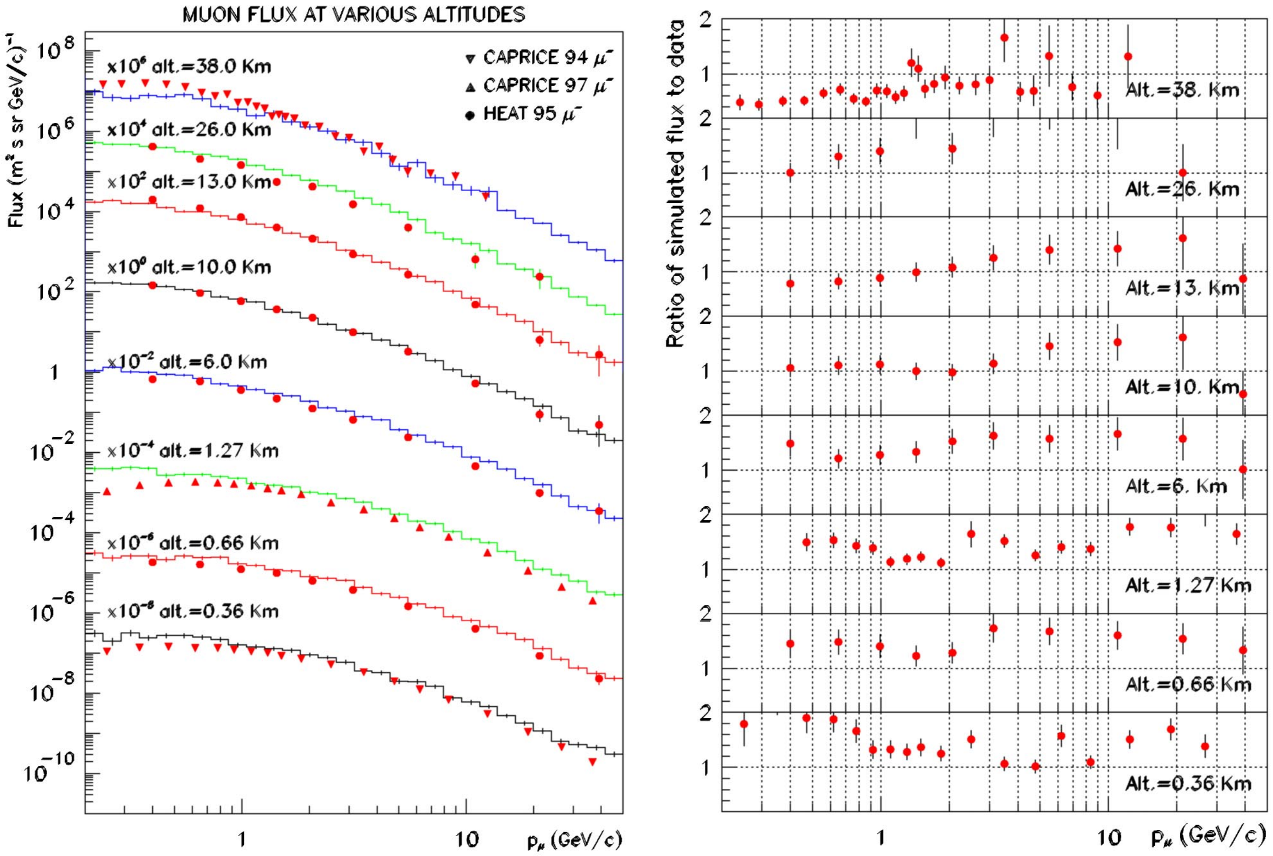

FIG. 1. Left: simulation results (histograms) for the negative muon flux at various altitudes in the atmosphere, compared to measurements (solid circles and triangles), from sea level up to about 38 km. See text for details. Right: ratio of simulated flux to the measurement for each data point.

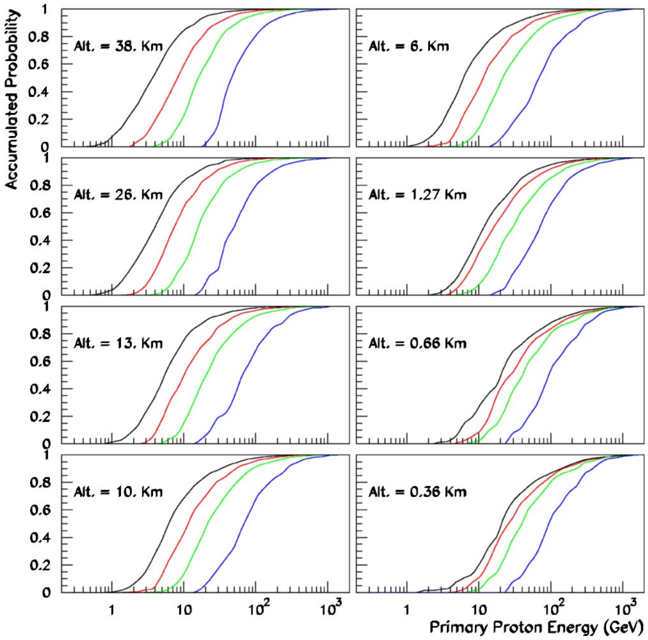

FIG. 2. CR proton kinetic energy distributions of the cumulative probability for producing downgoing muons in the energy bins of 0.2–0.4, 0.8–1.2, 2.0–4.0, and 8.0–12.0 GeV (from the left to the right), with zenith ($\theta_{zenith} \leqslant 15°$), for the altitudes indicated.

collisions, i.e., in the same reaction chain as neutrinos. A successful reproduction of the muon flux in the atmosphere is thus further support to the reliability of the neutrino flux calculated in the same framework, physical conditions, and computational environment. This is true as well for the electron-positron flux. For the latter, the present approach has allowed to successfully reproduce the AMS measurements of the $e^{\pm}$ flux and of their latitude dependence, in near Earth orbit recently [36] (see [50] for the $e^{\pm}$ in the atmosphere). The results on the muon flux are presented in this section.

It must be emphasized first that the muon experimental observables—namely, the energy dependence of the flux at various altitudes—are not available for neutrinos. Therefore they offer a test ground for flux calculations which is more sensitive to the various elements of the calculations than the neutrino observables discussed below. For this reason they deserve to be investigated with care.

A. Negative muons

Figure 1 shows the calculated muon flux compared to the data measured by the CAPRICE and HEAT experiments [31,32] at various altitudes (left) and the ratios of the simulated to measured values for each data point (right). The agreement between simulation results and data is quite good through the energy range investigated (0.5–50) GeV for all altitudes, from about the sea level to 38 km. It is especially good over the region from 10–26 km altitude where a large fraction of the neutrinos detected by underground detectors are produced (see below). A significant difference between simulation results and data is observed, however, at 38 km altitude for muon energies below 1 GeV. This might result from an underestimated production of low energy pions for CR incident energy below about 10 GeV, since the pion production cross section in this energy region is poorly constrained by the very little data available. Note, however, that relatively large uncertainties and variations of the measured values, are observed for the low energy muon data [51].

TABLE II. Mean incident CR proton energy (GeV) producing near vertical ($\theta_{zenith} \leqslant 15°$) downgoing muons in the specified energy bins and altitudes.

	Altitude (km)							
E_μ (GeV)	38	26	13	10	6	1.27	0.66	0.36
0.2–0.4	8.3	9.0	14.0	18.6	35.6	66.1	63.6	68.1
0.8–1.2	17.5	16.6	25.0	30.8	46.8	75.9	84.9	82.0
2.0–4.0	33.0	34.1	46.9	53.7	74.7	100.3	102.9	101.9
8.0–12.0	93.2	97.9	127.2	136.3	142.3	186.8	189.5	190.3

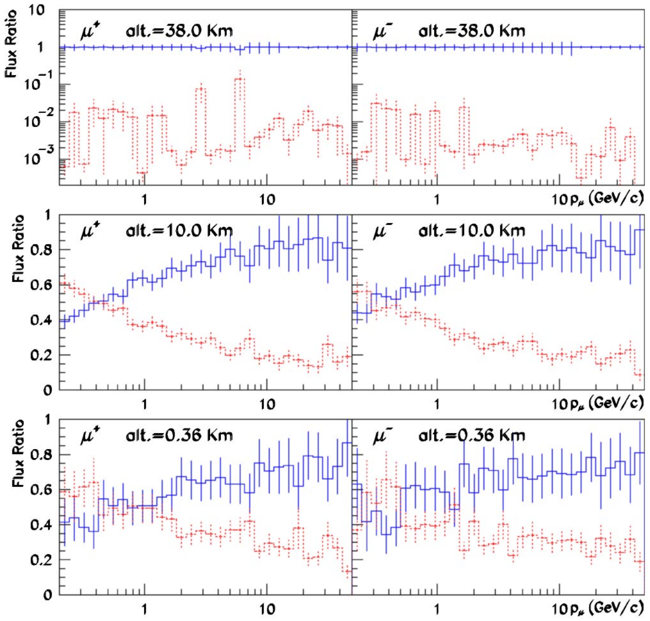

FIG. 3. Flux ratios for muons induced by the primary CR (proton+helium) flux (solid line), and by atmospheric secondaries (dotted lines), respectively, to the total flux, for three detection altitudes. The total flux are those from Fig. 1.

The energy distribution of the cumulated probability for the incident CR protons to produce downward-going muons close to zenith in different energy bins and for different altitudes, is illustrated in Fig. 2. The corresponding mean values of the primary proton energy are tabulated in Table II.

From Fig. 2, it is easy to see that the cumulative probability curves shift gradually toward the high energy region with the decreasing altitude, while the distances between the curves are compressed. This can be clearly seen as well from Table II. At 38 km altitude, the mean energies of primary protons producing 0.2–0.4 GeV muons and producing 8.0–12.0 GeV muons differ by a factor of about 11, this factor becoming about 7 at 10 km and 3 at around sea level.

Figure 2, Table II, and the following Fig. 3 and Fig. 18 show that (1) at the highest float altitude, the simulated muon flux is most sensitive to the pion production cross section used in the simulation and, hence, the higher altitude muon

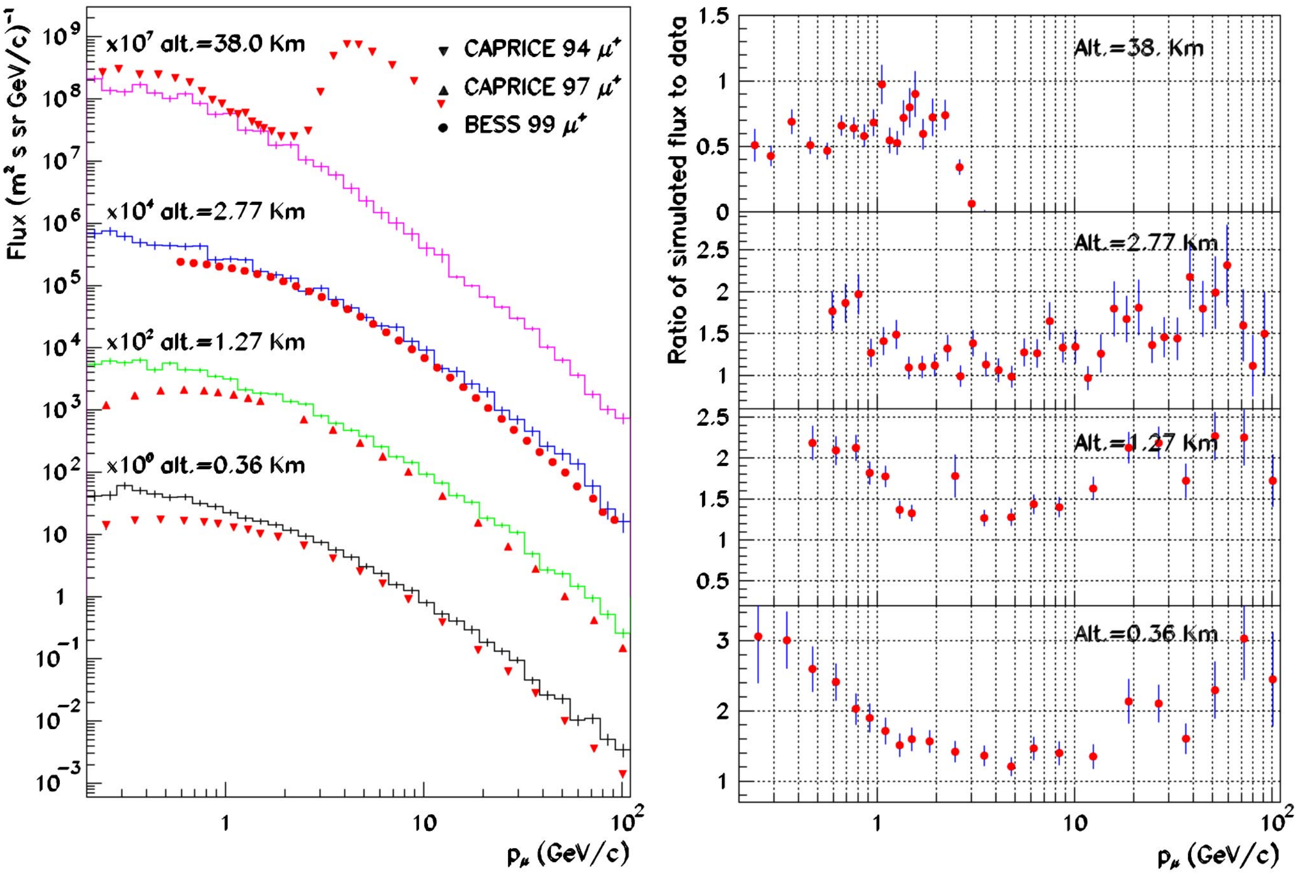

FIG. 4. Left: simulation results (histograms) for the positive muon flux at various altitudes in the atmosphere, compared with measurements (solid circles and triangles), from sea level up to 38 km, from Refs. [32,52]. See text for details. Right: ratio of simulated flux to the measurement for each data point.

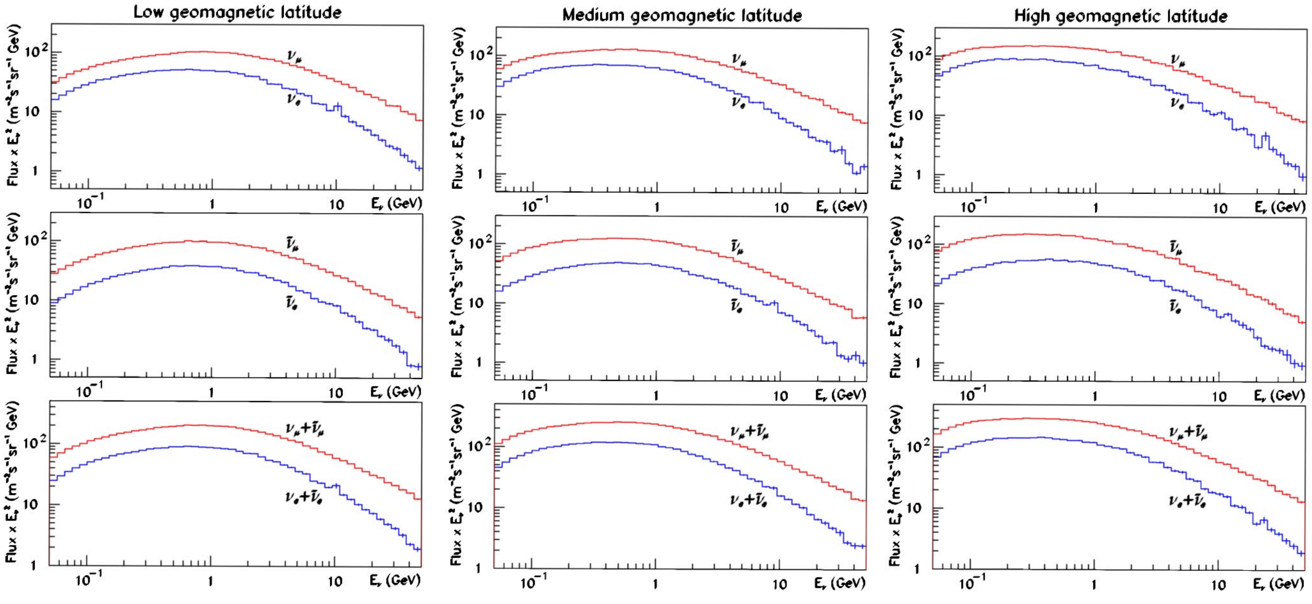

FIG. 5. Neutrino flux in three bins of geomagnetic latitude 0–0.5, 0.5–1, and 1–$\pi/2$ rad, averaged over a 4π solid angle. The error bars given in the figure and all the following figures are statistical unless specified otherwise.

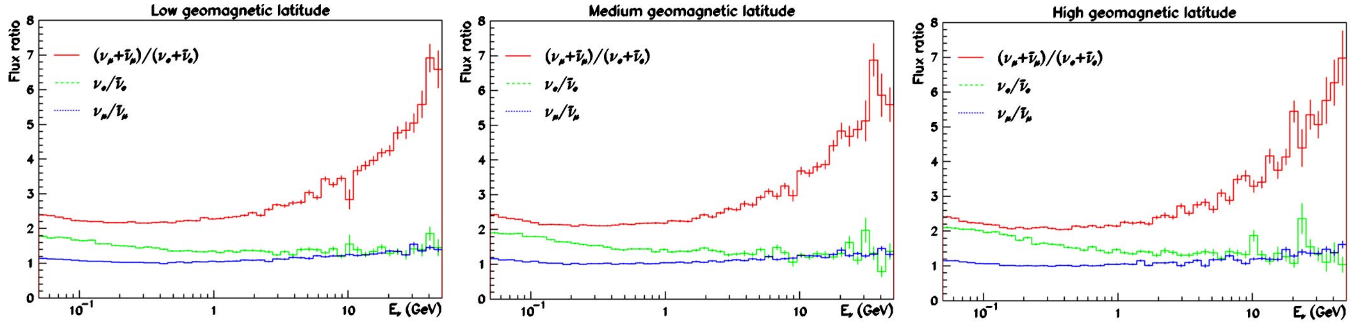

FIG. 6. Individual $\nu/\overline{\nu}$ and sum $(\nu_\mu+\overline{\nu}_\mu)/(\nu_e+\overline{\nu}_e)$ flux ratios, as in Fig. 5.

flux data can thus be taken as a good test of this cross section, and (2) in contrast, at around sea level, the low energy muon flux should be more sensitive to the proton-neutron production cross section because on the average:

(a) The low energy muon path length is roughly on the km scale, and the muons measured at sea level are thus produced at relatively low altitude.

(b) Above 10 km, about five collisions have occurred. In these collisions, more secondary protons or neutrons are produced, which can contribute largely to muons parent meson production.

B. Secondary proton contribution

The ratios of the muon flux originating from primary CRs and from secondaries respectively, to the total flux, are shown in Fig. 3. The flux are nearly vertical and the corresponding normalization area are the same as those shown in Fig. 1 for the three altitudes.

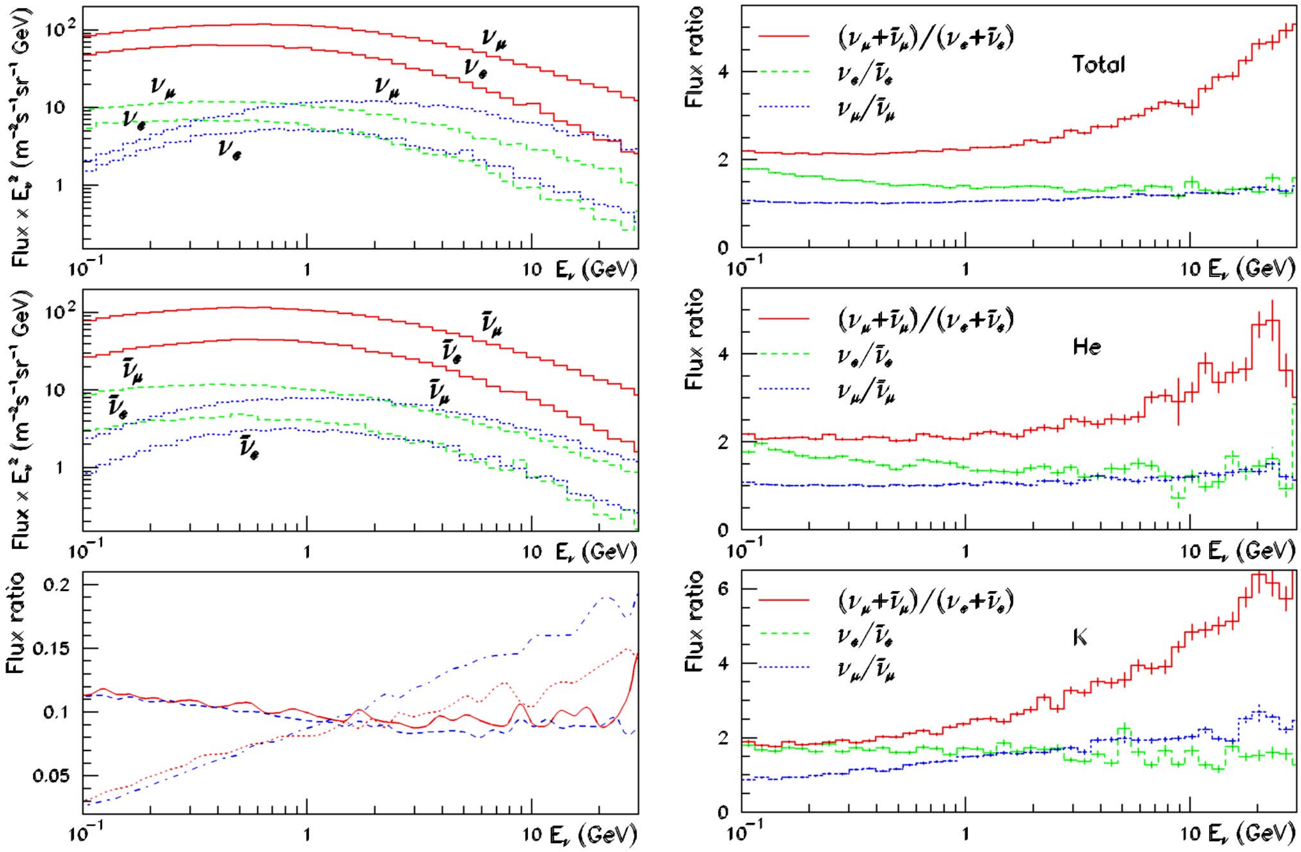

FIG. 7. Left up and middle: energy spectra of the CR helium flux contribution (dashed lines) and total kaon decay contribution (dotted lines), compared to the total flux (solid lines), for the ν and $\overline{\nu}$, neutrino flavors from top to bottom as indicated in the figure respectively. Left bottom: ratios of CR helium induced $(\nu_\mu+\overline{\nu}_\mu)$ flux to total $(\nu_\mu+\overline{\nu}_\mu)$ flux (solid line), CR helium induced $(\nu_e+\overline{\nu}_e)$ flux to total $(\nu_e+\overline{\nu}_e)$ flux (dashed line), kaon decay induced $(\nu_\mu+\overline{\nu}_\mu)$ flux to total $(\nu_\mu+\overline{\nu}_\mu)$ flux (dash-dot line), and kaon decay induced $(\nu_e+\overline{\nu}_e)$ flux to total $(\nu_e+\overline{\nu}_e)$ flux (dotted line). Right: flavor ratios for the same three contributions (Total, CR He induced, and kaon decay, from top to bottom respectively), averaged over 4π solid angle and integrated over the whole detection sphere. See text.

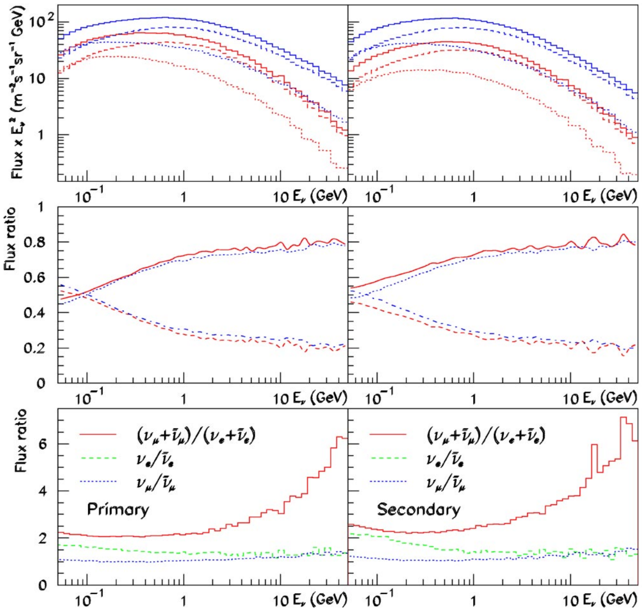

FIG. 8. Total neutrino flux, primary CR proton and helium directly induced neutrino flux, and secondary induced neutrino flux, averaged over whole detection sphere and over 4π solid angle. Top left: CR primary (dashed lines, up: ν_μ, down: ν_e), secondary (dotted lines, up: ν_μ, down: ν_e) contributions for ν_e and ν_μ, and total ν_e and ν_μ (solid lines, up: ν_μ, down: ν_e). Top right: CR primary (dashed lines, up: $\overline{\nu_\mu}$, down: $\overline{\nu_e}$), secondary (dotted lines, up: $\overline{\nu_\mu}$, down: $\overline{\nu_e}$) contributions for $\overline{\nu_e}$ and $\overline{\nu_\mu}$, and total $\overline{\nu_e}$ and $\overline{\nu_\mu}$ (solid lines, up: $\overline{\nu_\mu}$, down: $\overline{\nu_e}$). Middle: ratios of primary contributed flux to total flux and secondary contributed flux to total flux, for ν (left) and $\overline{\nu}$ (right). Dotted line: ratio of primary directly induced ν_μ ($\overline{\nu_\mu}$) to total ν_μ ($\overline{\nu_\mu}$). Solid line: ratio of primary directly induced ν_e ($\overline{\nu_e}$) to total ν_e ($\overline{\nu_e}$). Dash-dot line: ratio of secondary induced ν_μ ($\overline{\nu_\mu}$) to total ν_μ ($\overline{\nu_\mu}$). Dashed line: ratio of secondary induced ν_e ($\overline{\nu_e}$) to total ν_e ($\overline{\nu_e}$). Bottom: Flux ratios $\nu_e/\overline{\nu_e}$, $\nu_\mu/\overline{\nu_\mu}$, and $(\nu_\mu+\overline{\nu_\mu})/(\nu_e+\overline{\nu_e})$ for the primary directly induced (left panel) and secondary induced (right panel) components.

This figure shows, as could be expected from simple collision rank considerations, that in the whole muon energy range, at the highest float altitude, more than 98% muon flux originate from primary CRs. At intermediate altitudes, the flux induced by secondaries decreases continuously with the energy from about 60% at 0.2 GeV down to about 20% at 10 GeV, while at around sea level, the same trend is observed with a slower decrease with energy.

C. Positive muons

Figure 4 shows the calculated μ^+ flux compared to the measured data from the CAPRICE and BESS experiments. The agreement with the BESS 99 data at mountain altitude [52] is very good, but in the low (below 1.0 GeV) and high (beyond 10.0 GeV) energy range, the departure is obvious. This may result from the overestimation of the secondary-proton–neutron production cross section at low energy and pion-kaon production cross section at high energy.

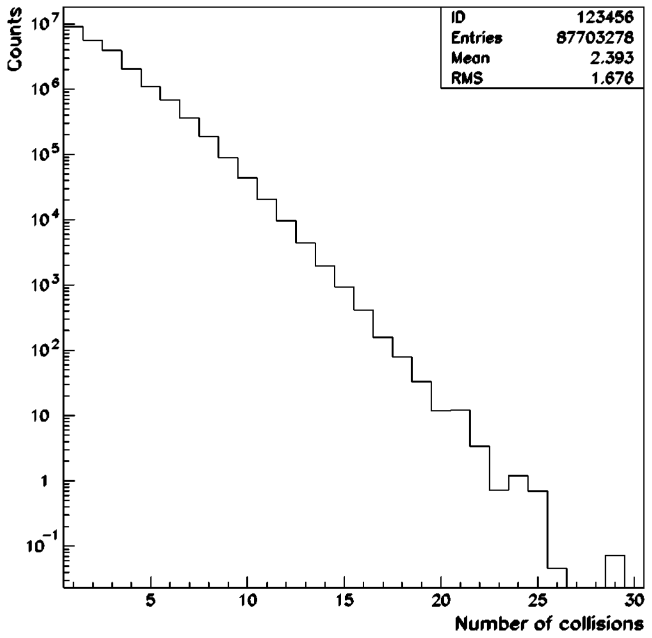

FIG. 9. Rank distribution of the neutrino producing collisions in the atmosphere. See text for details.

IV. PROPERTIES OF NEUTRINO SPECTRA

In this section, the characteristics of the simulated neutrino spectra, averaged over the whole detection surface, for three bins of geomagnetic latitude and integrated over a 4π solid angle, are described in details. The detection sphere is defined at 0.372 km, the altitude of the Super-Kamiokande detector. Some features having important implications for underground experiments are emphasized.

A. Absolute flux and flavor ratios

The calculated flux are shown in Fig. 5 for three bins of geomagnetic latitude. The corresponding ratios of flux are shown in Fig. 6, where it is seen that the flux increases with the geomagnetic latitude in the low energy ($<$ few GeV) range. At 0.1 GeV, the difference between the flux at low and high latitudes can be more than a factor of 2. However, this difference decreases with the increasing particle energy, vanishing beyond a few GeV. This reflects the effect of the geomagnetic field. Indeed, the mean primary particle energy associated with 1 GeV neutrino production is about 60 GeV (see below), a value at which the effects of the geomagnetic cutoff (GC) are small.

Figure 6 shows that the flavor ratios for low, middle, and high latitudes are very similar to each other. The $\nu_\mu/\overline{\nu_\mu}$ is flat through energy range, with its value near about 1.2. Here $\nu_e/\overline{\nu_e}$ decreases steadily from nearly 2 to about 1.2 overlap with $\nu_\mu/\overline{\nu_\mu}$ at high energy end, while $(\nu_\mu+\overline{\nu_\mu})/(\nu_e+\overline{\nu_e})$ rises up steeply above about 3 GeV. Large difference for $\nu_e/\overline{\nu_e}$ from the previous works is seen here (see [9,11] for comparisons).

These features can be easily understood in terms of the production of $\pi^+(K^+)$ and $\pi^-(K^-)$ and of the muon kine-

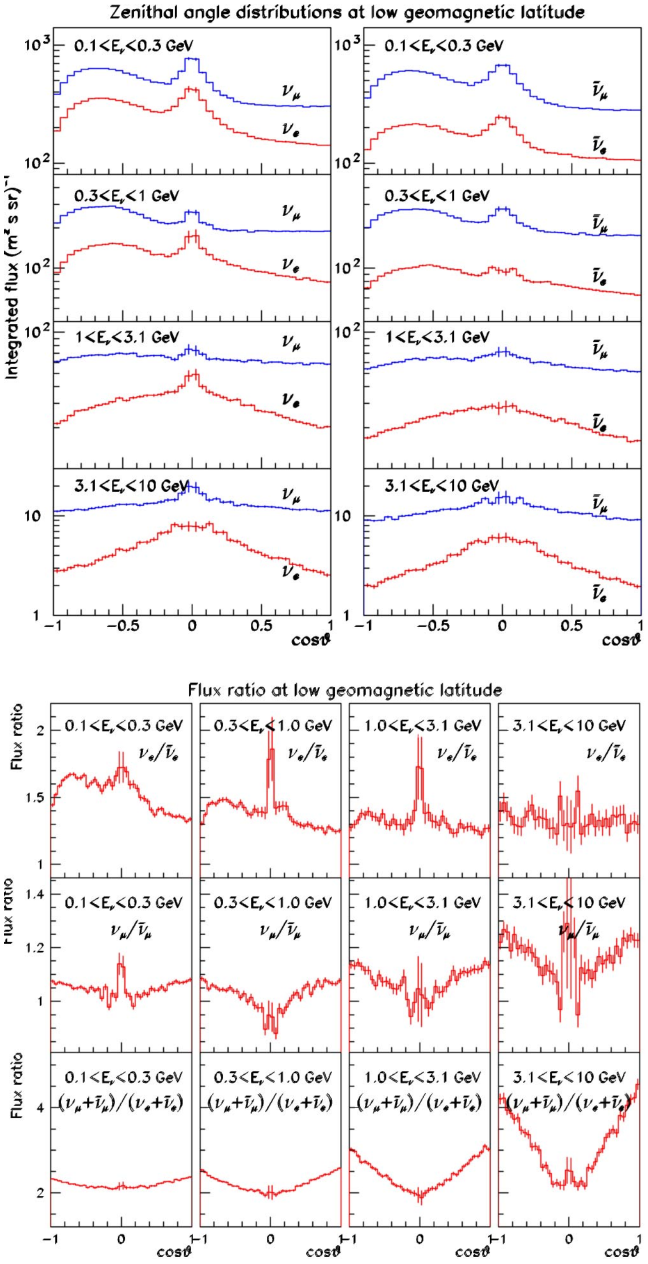

FIG. 10. Zenith angle distribution of the neutrino flux (top) and of the flavor ratios (bottom), in the indicated energy bins and for the indicated flavor, for low geomagnetic latitudes ($\theta_{lat}<0.5$ rad), and averaged over 4π solid angle. Here, the zenith angle is defined such that $\cos\theta=1$ corresponds to the downward direction.

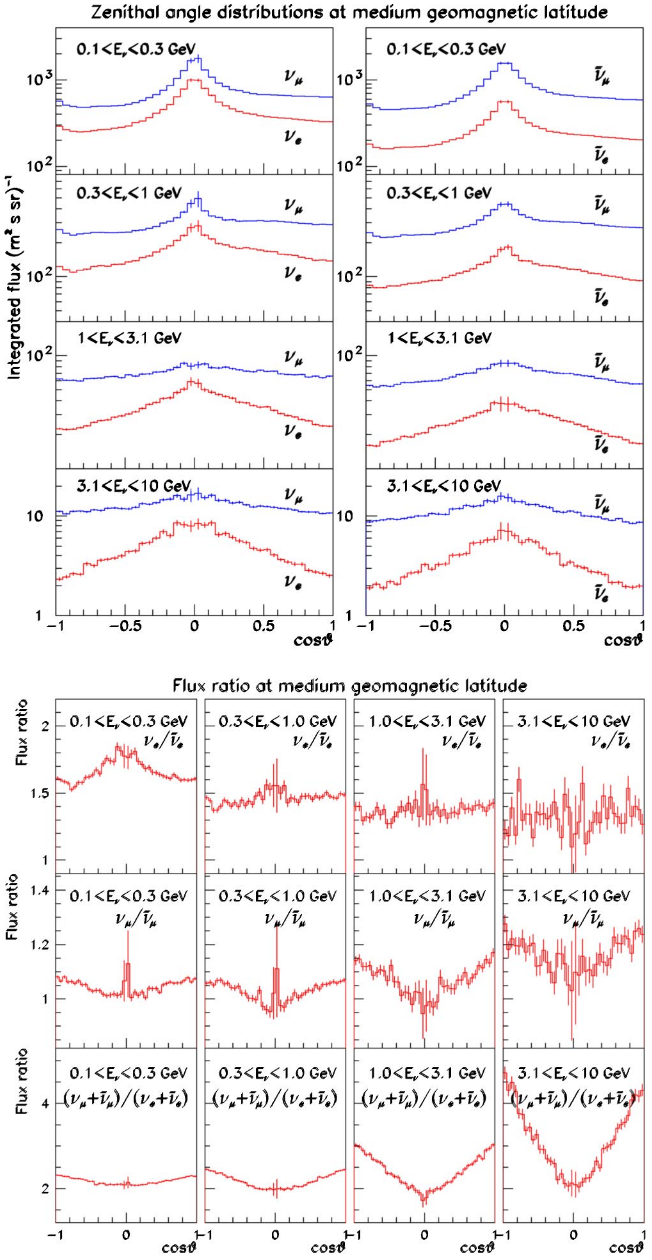

FIG. 11. Same as Fig. 10 for the geomagnetic latitudes $0.5<\theta_{lat}<1$.

matics. The ratio $\nu_e/\overline{\nu_e}$ is principally controlled by the ratio of $\pi^+(K^+)$ to $\pi^-(K^-)$. The ratio $(\nu_\mu+\overline{\nu_\mu})/(\nu_e+\overline{\nu_e})$ is sensitive to the muon decay kinematics. The variation of $\nu_\mu/\overline{\nu_\mu}$ with energy is thus determined by both $\pi^+/\pi^-(K^+/K^-)$ production ratios and the muon decay kinematics. Because of the Lorentz time dilation, more higher energy muons do not decay while crossing the atmosphere. Hence, the $\nu_e(\overline{\nu_e})$ production (resulting from muon decay) is lesser than for $\nu_\mu(\overline{\nu_\mu})$, since a ν_μ has been produced in association with the μ in the π decay, resulting in a $(\nu_\mu+\overline{\nu_\mu})/(\nu_e+\overline{\nu_e})$ ratio rising up with the neutrino energy.

Here, two points should be noted. First, the $\nu_e/\overline{\nu_e}$ ratio at low energy should be expected to be larger since the largest production ratio of π^+/π^- is at low incident CR energy (see [53], for example). Second, the $\nu_e/\overline{\nu_e}$ ratio should decrease to overlap with $\nu_\mu/\overline{\nu_\mu}$ at high energy with their values approaching to 1.0. This is because at high incident primary energy, the production ratio of π^+/π^- and K^+/K^- approaches to 1.0 [54], and most of the high energy muons from which the high energy ν_e and $\overline{\nu_e}$ come will not decay before reaching the detection sphere. So the ν_μ flux is dominated by the π^+ decay while the $\overline{\nu_\mu}$ flux is dominated by π^- decay. And hence, at very high energy,

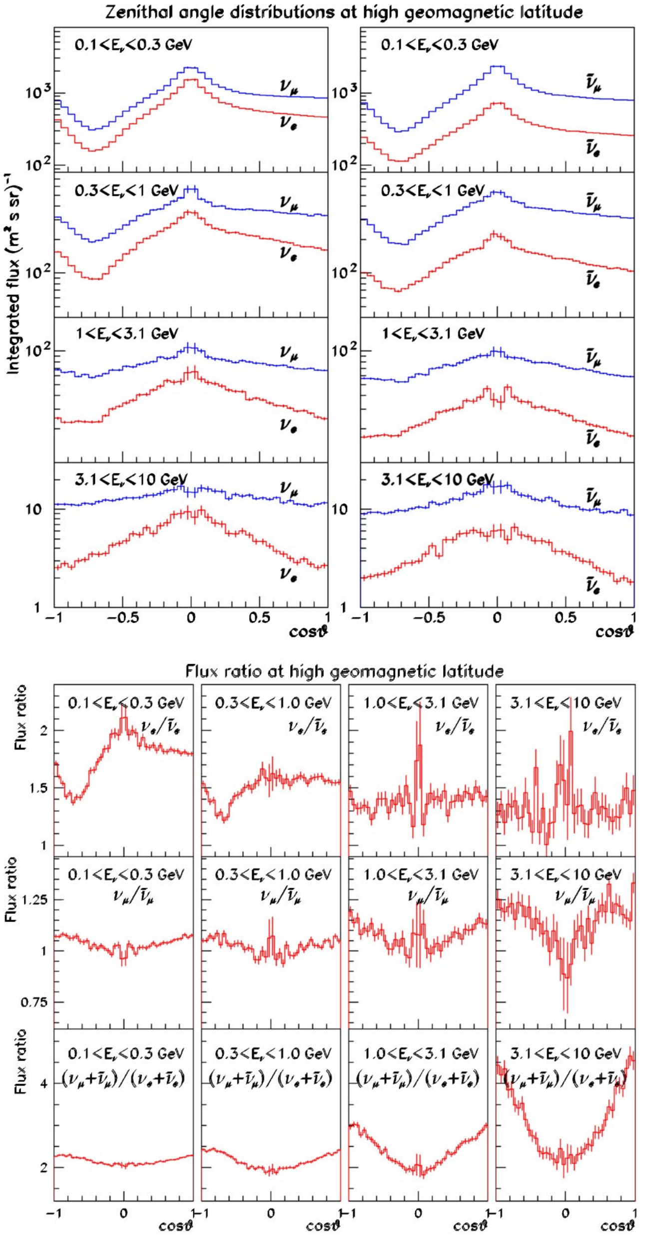

FIG. 12. Same as Fig. 10 for the geomagnetic latitudes $1 < \theta_{lat} < \pi/2$.

$$\nu_e/\overline{\nu_e} \approx \nu_\mu/\overline{\nu_\mu} \approx \pi^+(K^+)/\pi^-(K^-).$$

Such characteristics can be seen clearly in Fig. 6.

B. Contribution from the incident CR He flux

The calculated total neutrino flux is compared in the left of Fig. 7 with the contribution induced by the CR helium (He) flux and with the total kaon decay contribution. The corresponding flavor ratios are also shown in the same figure (right panel), where it is seen that the contribution of the CR He flux to the total neutrino flux is about 10% through the whole energy range.

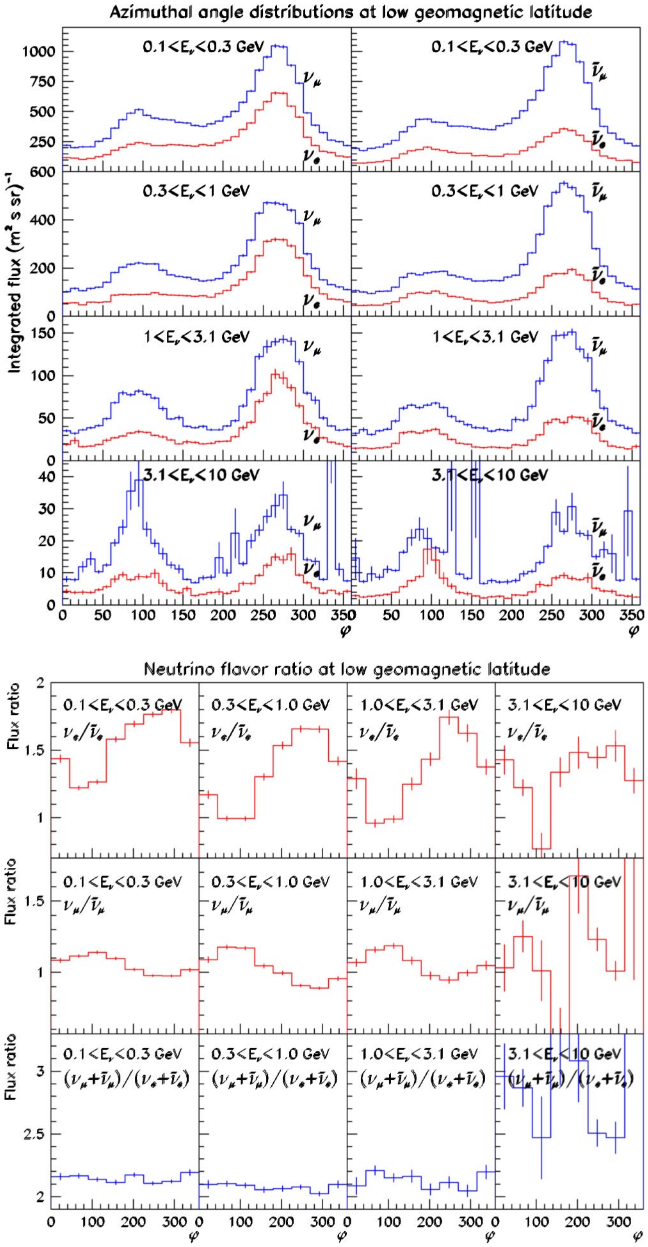

FIG. 13. Azimuth angle distribution of the neutrino flux (top) and of the flavor ratios (bottom), in the indicated energy bins and for the indicated flavor, for low geomagnetic latitudes ($\theta_{lat} < 0.5$ rad) and averaged over 4π solid angle. The angle convention is $\phi = 0°, 90°$ for geomagnetic south and east, respectively.

This contribution is constrained by both the CR He spectral abundance and the He-induced pion multiplicity in nuclear collisions. Around 20 GeV per nucleon incident energy, where the neutrino production around 1 GeV is maximum (see discussion below and [15]), the CR He flux is about 5% of the p flux, this fraction decreasing slowly with increasing primary energy. Experimentally, the pion multiplicity increases with the mass of the projectile according to a known law [46]. For the $\alpha + \mathrm{C}$ reaction at 4 GeV/nucleon, it is about 3 times the $p + \mathrm{C}$ value at the same incident energy [44]. These numbers are in qualitative agreement with the 10% contribution to the neutrino flux found to arise from the

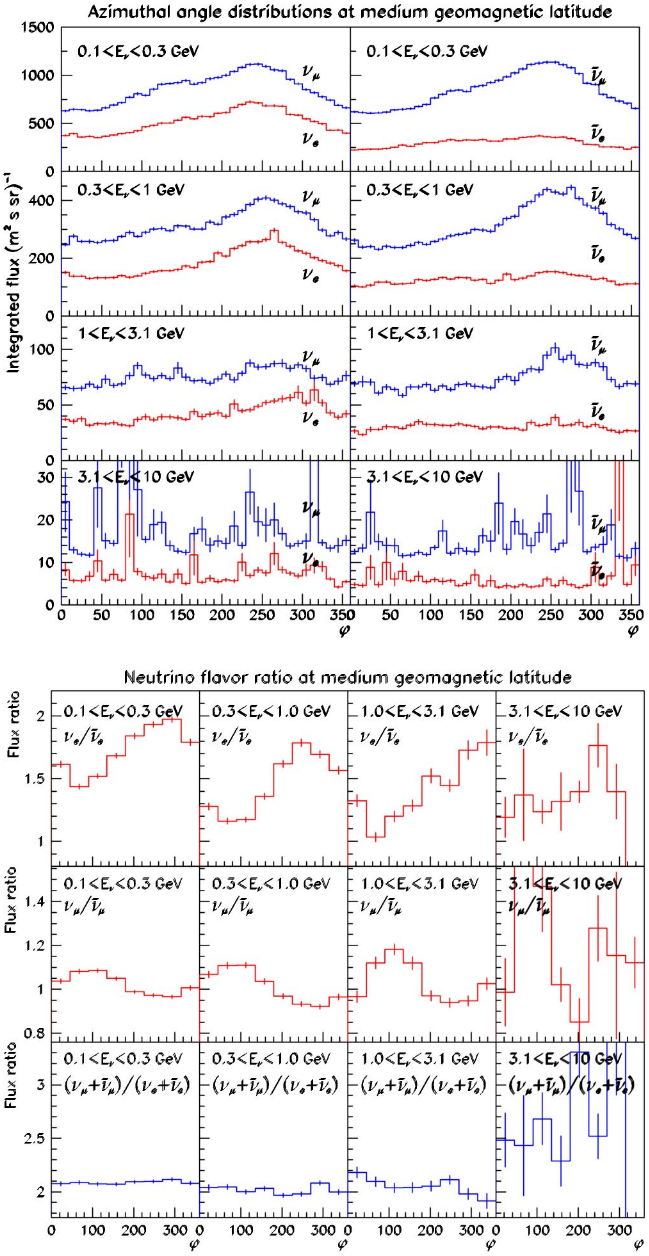

FIG. 14. Same as Fig. 13 for intermediate geomagnetic latitudes $(0.5<\theta_{lat}<1)$.

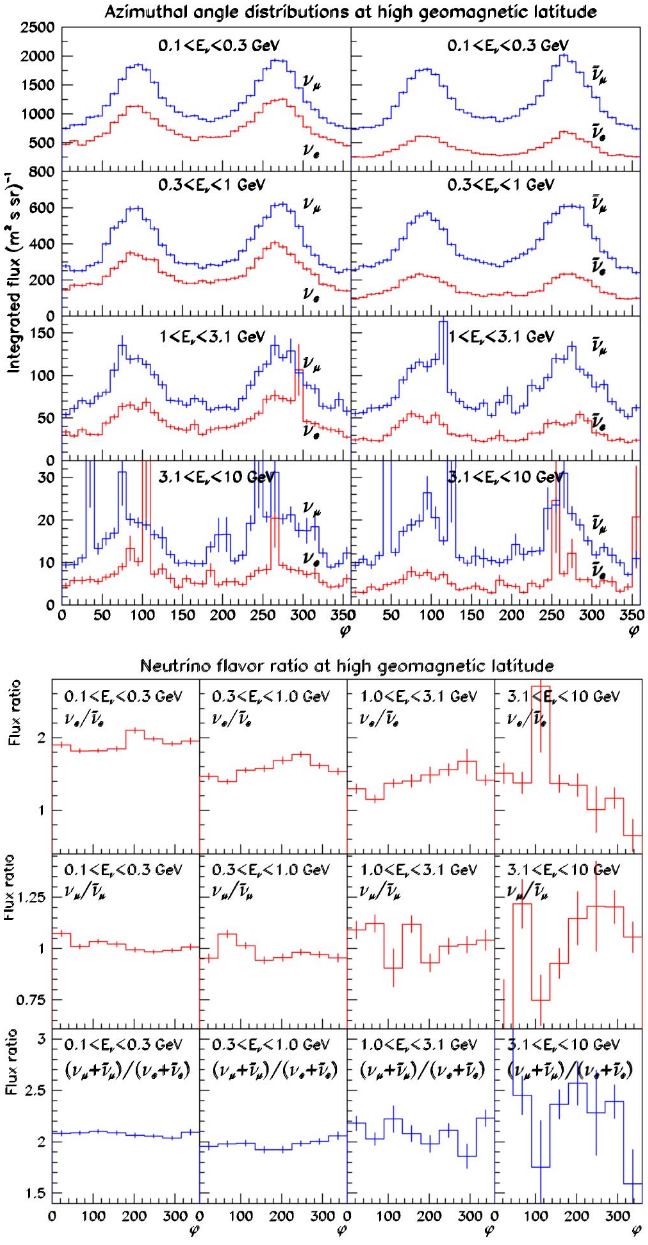

FIG. 15. Same as Fig. 13 for high geomagnetic latitudes $(1<\theta_{lat}<\pi/2)$.

He flux, assuming that the proton-induced helium contribution is small. This result is also consistent with the previous work on the AMS lepton data by the authors [36].

The difference between the contributions of CR He to the $(\nu_e+\overline{\nu}_e)$ and $(\nu_\mu+\overline{\nu}_\mu)$ flux ratios is very small as seen in the lower left of Fig. 7. For the flavor ratio of the He flux contributions shown in the middle right of Fig. 7, they have a similar energy dependence as the total flux, as it could be expected (top).

C. Contribution from secondary kaons

At low energies the neutrino flux mostly results from π decay in account of the dominance of the pion production. The kaon decay contribution increases, however, with increasing incident energy and the K production cross section, and finally dominates the production for very high energy neutrinos. This is shown in the left of Fig. 7 where the kaon decay contribution to the total neutrino flux (bottom left) is seen to increase continuously from about 2%–3% at 0.1 GeV up to $\approx$15% for $(\nu_e+\overline{\nu}_e)$, and $\approx$20% for $(\nu_\mu+\overline{\nu}_\mu)$, above 20 GeV. These results are in agreement with [9,11].

The energy dependence of the flavor ratio for the kaon decay contribution to the neutrino flux is a little different from the averaged value (bottom right panel in Fig. 7). The ratio $\nu_e/\overline{\nu}_e$ decreases slowly with increasing energy from 1.7 at 0.1 GeV down to about 1 at 10 GeV, while $\nu_\mu/\overline{\nu}_\mu$ increases continuously from 0.9 at 0.1 GeV up to about 2.1 at

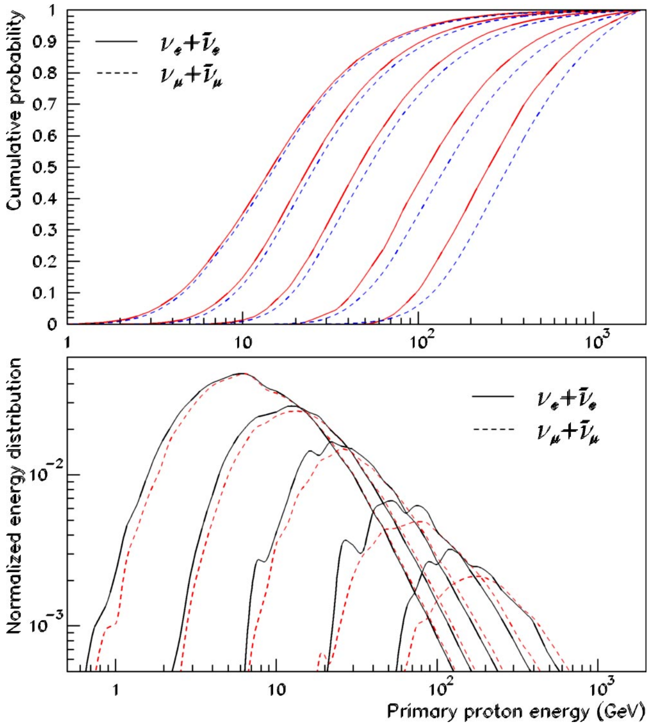

FIG. 16. The cumulative (top) and normalized (bottom) primary proton energy distribution for $\nu_e+\overline{\nu_e}$ (solid lines) and $\nu_\mu+\overline{\nu_\mu}$ (dashed lines) production in five energy bins 0.28–0.32, 0.8–1.2, 2.8–3.2, 8.0–12.0, and 20.0–30.0 GeV from the left to the right, respectively.

10 GeV. In contrast with the individual flavor ratios, the $(\nu_\mu+\overline{\nu_\mu})/(\nu_e+\overline{\nu_e})$ ratio grows rapidly from 1.8 at 0.1 GeV up to about 5 at 10 GeV. These differences principally result from the K^+ to K^- production ratio being larger than for π^+ to π^- [55].

Another noticeable feature of the kaon decay contribution is that, below 0.4 GeV neutrino energy, the ratio $(\nu_\mu+\overline{\nu_\mu})/(\nu_e+\overline{\nu_e})$ is less than 2. This can be understood from the $K_{3e\nu}$ decay mode having always larger a branching ratio than the $K_{3\mu\nu}$ mode. In particular, for K_L^0, the $K_{3e\nu}$ channel is the dominant decay mode [48].

D. Contribution of atmospheric secondaries to the neutrino flux

The contribution of the atmospheric secondary flux is compared in Fig. 8 with that of the primary component. It is seen that, at 0.1 GeV, about 50% of the neutrinos come from secondary proton- and neutron-induced reactions, this fraction decreasing to about 20% at 50 GeV.

The ratio of the secondary contribution, $\nu_e/\overline{\nu_e}$, is larger than for the primary contribution. This is because of the larger flux of low energy secondaries due to the larger π^+/π^- production ratio at low incident energy.

The distribution of the rank in the cascade of the neutrino producing collision is plotted in Fig. 9 [35]. The rank is defined as the number of collisions taking place before the neutrino is produced. It is 1 when the neutrino is produced from the incident cosmic ray interaction. The figure shows that, on the average, about 2.4 collisions occur for the parent pion or kaon to be produced.

E. Zenith angular distribution and geomagnetic latitude dependence of the neutrino flux

The zenith angle distributions are shown in Figs. 10, 11, and 12 for the geomagnetic latitude bins (rad) 0–0.5, 0.5–1, and $1-\pi/2$, respectively, and for several energy bins between 0.1 and 10 GeV.

The figures show that the zenith angle distributions for downward going neutrinos ($\cos\theta>0$) have about the same shape for all the energy bins, while for upward going neutrinos, they display quite different shapes for the low energy bins, showing (a) a clear maximum for low latitudes, (b) a flat shape at middle latitude, and (c) a deep minimum at high latitudes. This can be understood by considering the following two particular cases: (1) For a detection point at the north pole, the $(\pi/4)$ zenith angle $\cos\theta\sim-1/\sqrt{2}$ points to particles coming from the equatorial region where the geomagnetic cutoff for CR particles is highest. The neutrino flux is then expected lower for this angle. This effect is more sensitive for the low energy region of the neutrino spectrum. (2) Conversely, for a detection point at the equator, the zenith angle $\cos\theta\sim-\sqrt{2}/2$ points to particles coming from the poles (although for a narrow azimuthal angle region only) where the GC is minimum and hence the observed neutrino flux is expected larger around this angle.

The zenith angle dependence of the flavor ratios is modulated clearly by the π^+/π^- production ratio, GC, and the muon decay kinematics. Interestingly, in low energy bins, the $\nu_e/\overline{\nu_e}$ dependence on the zenith angle displays a similar behavior as observed for the flux. In addition to its dependence on the GC, this feature is also related to the pion multiplicity. Because the production ratio for π^+ to π^- is larger below 10 GeV [47], the incident CR flux within this energy range, which contributes a large fraction of low energy neutrinos, is very sensitive to the GC, and hence the $\nu_e/\overline{\nu_e}$ changes accordingly with the geomagnetic latitude and zenith angle.

The $\nu_\mu/\overline{\nu_\mu}$ distribution is flat in low energy bins but behaves similarly as $(\nu_\mu+\overline{\nu_\mu})/(\nu_e+\overline{\nu_e})$ at high energies. For

TABLE III. Mean incident kinetic energy in GeV of the CR protons producing neutrinos in the energy bins E_ν.

E_ν (GeV)	0.1–0.2	0.28–0.32	0.8–1.2	2.8–3.2	8.0–12	20–30	0.1–30
$\langle E_p\rangle_{\nu_e+\overline{\nu_e}}$	30.1	37.1	57	102	220	405	39
$\langle E_p\rangle_{\nu_\mu+\overline{\nu_\mu}}$	31	39	64	120	271	498	43

TABLE IV. Mean neutrino energies $\langle E_\nu \rangle$ produced by CR protons within kinetic energy bins E_p. Neutrinos with energy below 0.05 GeV are not included in the average.

E_p (GeV)	0.2–10	10–30	30–50	50–200	200–500	500–2000	0.20–2000
$\langle E_{\nu_e+\overline{\nu}_e} \rangle$	0.25	0.40	0.52	0.67	0.93	1.14	0.42
$\langle E_{\nu_\mu+\overline{\nu}_\mu} \rangle$	0.25	0.40	0.56	0.81	1.36	2.19	0.48

both the downward and upward flux, it is expected that the $\nu_\mu/\overline{\nu}_\mu$ ratio approaches asymptotically the π^+/π^- production cross section ratio at the limit of infinite muon lifetime.

The $(\nu_\mu+\overline{\nu}_\mu)/(\nu_e+\overline{\nu}_e)$ ratio displays a clear dependence on the zenith angle, with a symmetric up-down distribution, increasing from a minimum around the horizontal direction to a maximum for vertical incidences, the larger the energy bin, the more dramatic being the variation. This is because muons coming in horizontal directions have long path lengths in the atmosphere and then enough time to decay, producing a $\nu_\mu-\overline{\nu}_\mu$ pair and a $\nu_e(\overline{\nu}_e)$ for each pion decay. The situation is different for muons moving downward or upward, since the flight path available is much shorter. In this case, a fraction of high energy muons do not decay before reaching Earth and then do not contribute to the $\nu_e(\overline{\nu}_e)$ flux, wherefrom a larger $(\nu_\mu+\overline{\nu}_\mu)/(\nu_e+\overline{\nu}_e)$ ratio. The larger the muon energy, the larger the effect.

F. Azimuth angle distributions and geomagnetic latitude dependence

The azimuth angle distributions of the neutrino flux and of the flavor ratios are shown in Figs. 13 to 15 in bins of neutrino energy (0.1–0.3, 0.3–1, 1–3.1, 3.1–10 GeV) and for three bins of geomagnetic latitude (in absolute value): 0–0.5, 0.5–1, and $1-\pi/2$ rad, respectively.

It can be observed in these figures that the azimuth angle distributions display a significant dependence on the latitude considered. For low geomagnetic latitudes (Fig. 13), the distributions are dominated by two peaks located symmetrically at the east (E) and west (W) azimuth angles, but with different heights. These latter features are clearly related to the dipole nature of the Earth magnetic field for the E and W peaking and to the GC for the EW asymmetry. It is also seen that the EW asymmetry decreases as expected with the increasing energy.

For intermediate geomagnetic latitudes (Fig. 14), the west peak appears dampen and wider compared to low latitudes, while the east peak is even fainter and disappears in the high energy bins. The two-peak pattern reappears with nearly equal heights at high latitude (Fig. 15). This latter symmetry was expected since the GC disappears in the polar region.

For the azimuth angle distributions of the flavor ratios, it can be noted that the $\nu_e/\overline{\nu}_e$ ratio is strongly EW asymmetric with a broad enhancement on the west side at low and intermediate latitudes. The opposite trend is observed for the $\nu_\mu/\overline{\nu}_\mu$ ratio, while the $(\nu_\mu+\overline{\nu}_\mu)/(\nu_e+\overline{\nu}_e)$ ratio is found to be almost structureless at all latitudes.

The reason for these features is similar to that of zenithal angle dependence. The latitude dependence of the zenith and azimuth angle distributions reflects the characteristic of the geomagnetic field and reminds us that an appropriate treatment of the geomagnetic field is required to account for the upward-going muon event data and for the east-west asymmetry. Besides, detailed simulation for detectors at different locations is needed to provide a sensitive investigation of the geomagnetic dependence of the measurements.

G. Cosmic ray parent proton energy distributions

The incident CR proton energy distribution inducing the neutrino flux is shown in Fig. 16 for neutrino energies around 0.3, 1, 3, and 10 GeV. The distributions are given for $\nu_e+\overline{\nu}_e$ and $\nu_\mu+\overline{\nu}_\mu$. They are averaged over the whole detection sphere and 4π solid angle and presented as cumulative probabilities for neutrinos within the energy bins to be produced by protons with an energy below the value given in abscissa and energy distributions normalized to 1.

At variance with the results of [18], the mean energy of the primary proton flux producing 0.3 GeV $(\nu_e+\overline{\nu}_e)$ obtained in these calculations appears to be hardly smaller than for $(\nu_\mu+\overline{\nu}_\mu)$ in the same energy bin. The difference becomes larger with increasing energy, however. The mean values of the proton distributions of the figure are given in Table III.

Table IV gives, for comparison, the mean energy of the $(\nu_e+\overline{\nu}_e)$ and $(\nu_\mu+\overline{\nu}_\mu)$ neutrino spectrum produced by protons within the indicated energy bins. The mean neutrino energy value is found to be smaller for $(\nu_e+\overline{\nu}_e)$ than for $(\nu_\mu+\overline{\nu}_\mu)$ for the higher energy bins of the incident protons. This is consistent with the fact that in the decay chain $\pi^\pm \rightarrow \mu^\pm+\nu_\mu(\overline{\nu}_\mu)$, $\mu^\pm \rightarrow e^\pm+\nu_e(\overline{\nu}_e)+\overline{\nu}_\mu(\nu_\mu)$, the $\nu_e(\overline{\nu}_e)$ particle shares the energy of decaying $\mu^\pm$ which momentum

TABLE V. Mean neutrino production altitudes (km) corresponding to different neutrino energy bins.

E_ν (GeV)	0.1–0.2	0.28–0.32	0.8–1.2	2.8–3.2	8.0–12	20–30
$\langle \mathrm{Alt}_{\nu_e+\overline{\nu}_e} \rangle$	18.	18.5	18.3	17.1	16.1	15.3
$\langle \mathrm{Alt}_{\nu_\mu+\overline{\nu}_\mu} \rangle$	18.1	19	19.6	19.6	19.3	19.1

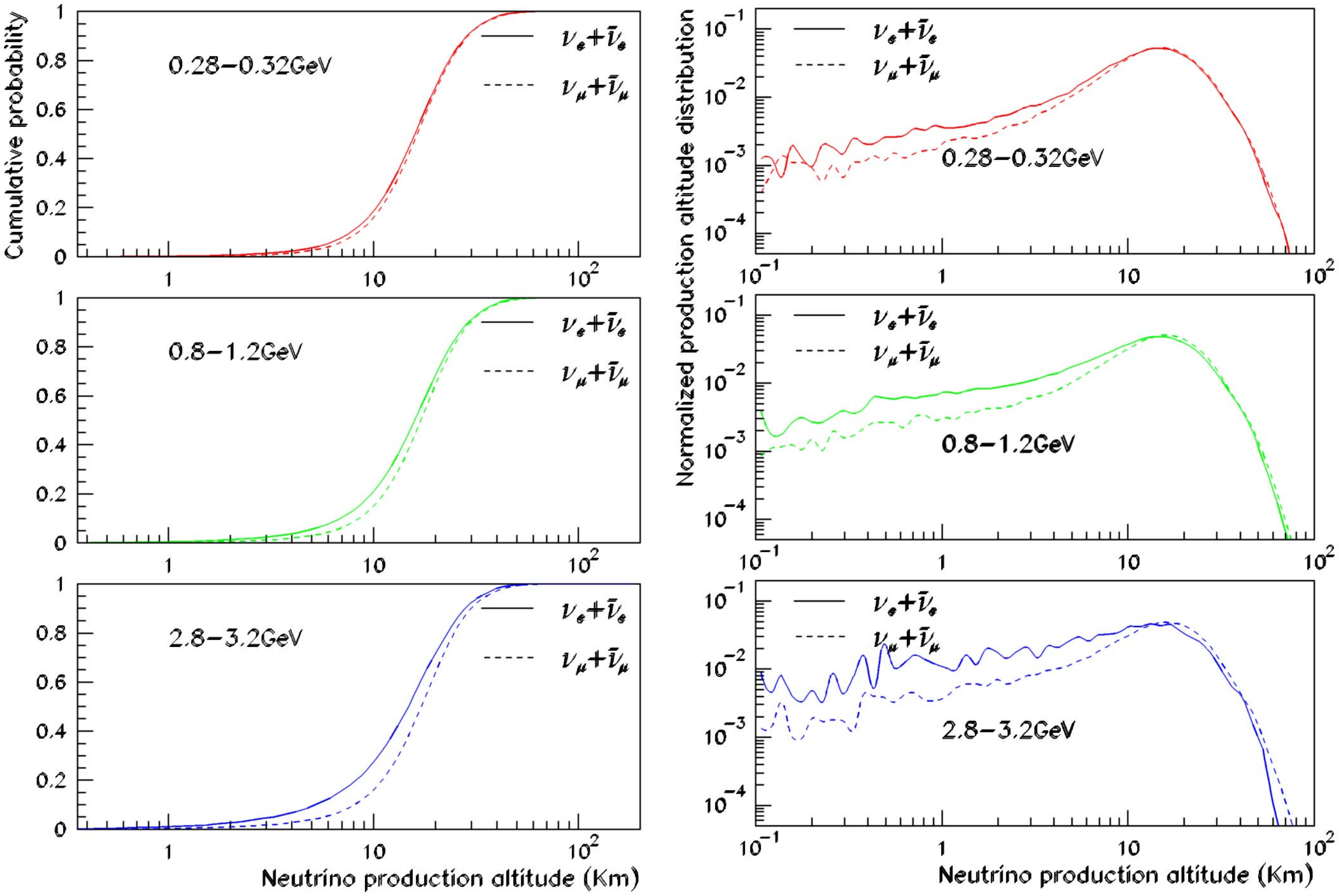

FIG. 17. Cumulative (left) and normalized (right) $\nu_e+\overline{\nu_e}$ and $\nu_\mu+\overline{\nu_\mu}$ production altitude distributions, for different neutrino energy bins, averaged over the whole detection sphere and 4π solid angle.

is equal to that of the first $\nu_\mu(\overline{\nu_\mu})$ in $\pi^\pm$ center-of-mass frame with $e^\pm$ and another $\overline{\nu_\mu}(\nu_\mu)$. The energy-momentum conservation implies that the $\nu_e(\overline{\nu_e})$ energy is on the average smaller than the mean energy of the two $\overline{\nu_\mu}(\nu_\mu)$.

In Fig. 16, it is seen that low energy primary protons contribute more to $(\nu_e+\overline{\nu_e})$ than to the same energy $(\nu_\mu+\overline{\nu_\mu})$ production. This is easy to understand if we note that higher energy muons which are produced by higher energy primaries on the average do not contribute to electron neutrinos, but accompany them; a muon neutrino has been created in pion decay. Even at low energy, this process can happen near the detection surface, and so the mean primary proton energy for muon neutrino production is raised up.

H. Neutrino production altitudes

The distribution of the neutrino production altitude is plotted in Fig. 17, where about 90% neutrinos appear to be produced between 5 and 40 km altitude, with the most probable production altitude being within the 15–20 km range. These numbers are consistent with the previous 1-dimensional analysis [56]. Below a few kilometers, the production distribution tends to flatten, governed by the absorption rate, while beyond 40 km, it drops following the atmospheric density profile.

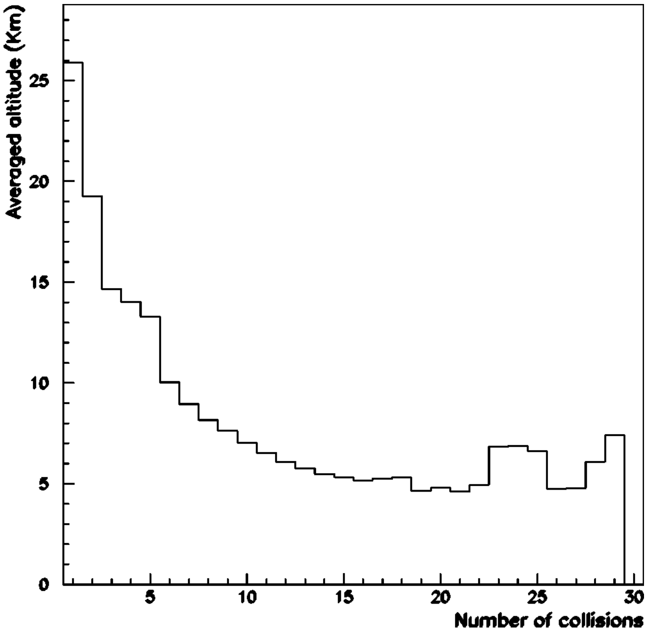

FIG. 18. Average collision altitude of the Nth collision versus collision number N.

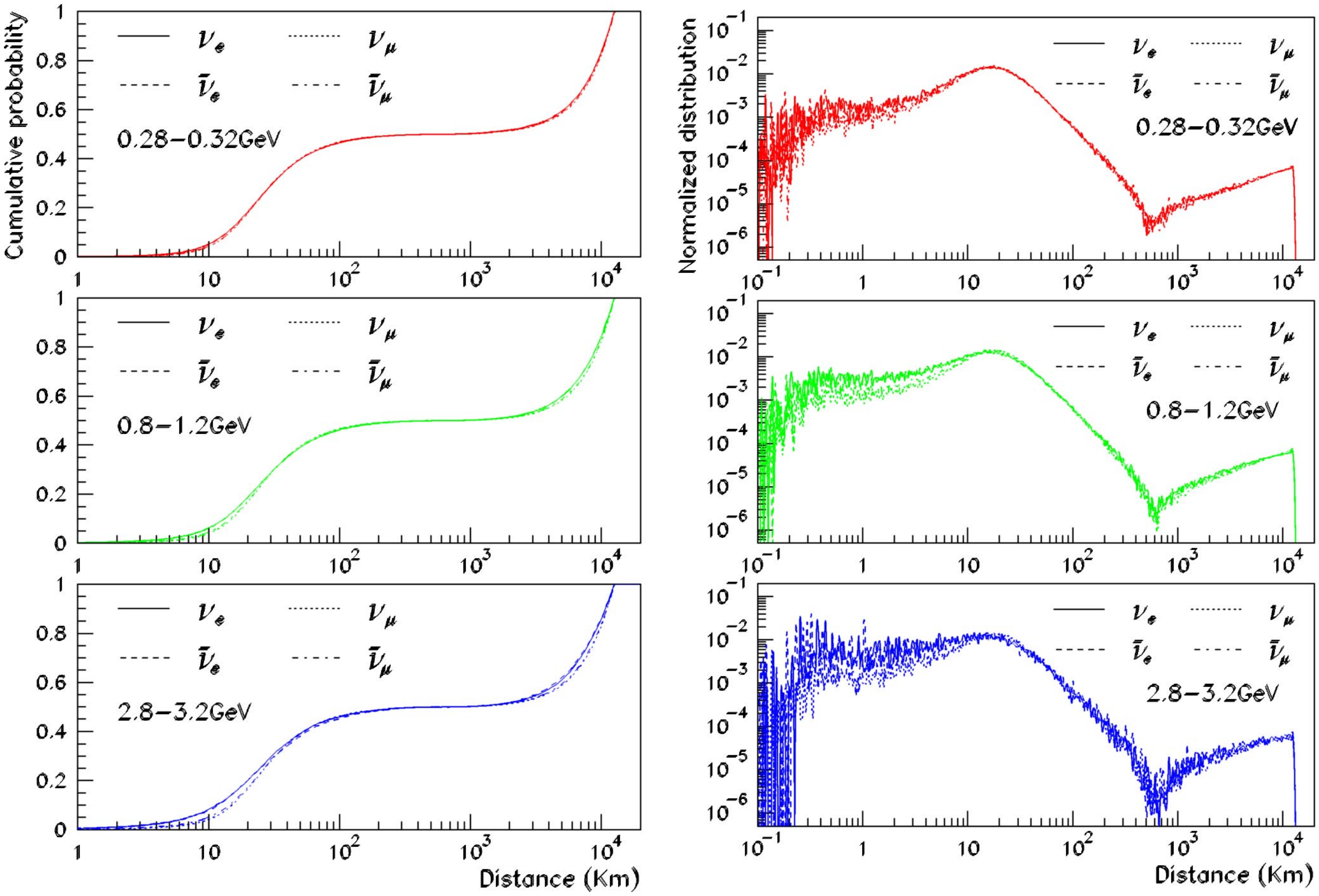

FIG. 19. Cumulative (left) and normalized (right) ν_e, $\overline{\nu_e}$, ν_μ, and $\overline{\nu_\mu}$ flying distance distributions, for different neutrino energy bins, averaged over the whole detection sphere and 4π solid angle.

Table V lists the average production altitudes corresponding to different neutrino energy bins. The average electron neutrino production altitude appears to be a little below that of muon neutrinos, because muons can fly over a certain distance—on the km scale for the energies considered here—before decaying into electrons.

The distribution of the altitude where the first interaction of the incidents CRs with atmosphere takes place was found to have a mean value of about 26 km on average, 23 km for nearly vertical ($0.9 \leqslant \cos\theta \leqslant 1.0$ at the first collision point), and 38 km for nearly horizontal ($0.0 \leqslant \cos\theta \leqslant 0.1$ at the first collision point) CRs, with no other selection cut than a produced neutrino reaching the detection sphere eventually.

Figure 18 shows the distribution of the averaged altitude at which the Nth collision occurs in the neutrino-producing reaction chain as a function of the number N of the collision.

It can be observed that, on the average, the second collision takes place around 19 km and the third collision around 15 km. In addition, below 4 km altitude, there is almost no meson producing collision because the initial CR energy has been damped through the cascade and most particles produced below this altitude are below the pion production threshold.

I. Neutrino flying distance

Figure 19 shows the distribution of the neutrino flying distance between production and detection point. The distributions of the mean values as a function of the cosine of the zenith angle are plotted in Fig. 20 for four neutrino energy bins and for the four neutrino flavors. These distributions are very similar to those obtained in [57].

The degeneracy of the curves shown in Fig. 20 for the four flavors can be easily understood by looking at Fig. 17 and Table V; the scales of the peak production altitude and the difference of the production altitude for different flavors

TABLE VI. Mean neutrino production angle (deg) relative to the CR particle direction at the first collision, for different neutrino energy bins.

E_ν (GeV)	0.1–0.2	0.28–0.32	0.8–1.2	2.8–3.2	8.0–12	20–30	0.1–30
$\langle\theta_{CR-(\nu_e,\overline{\nu_e})}\rangle$	28.3	16.7	7.3	3.2	1.4	0.69	20.2
$\langle\theta_{CR-(\nu_\mu,\overline{\nu_\mu})}\rangle$	27.7	15.7	6.6	2.7	1	0.46	19.1

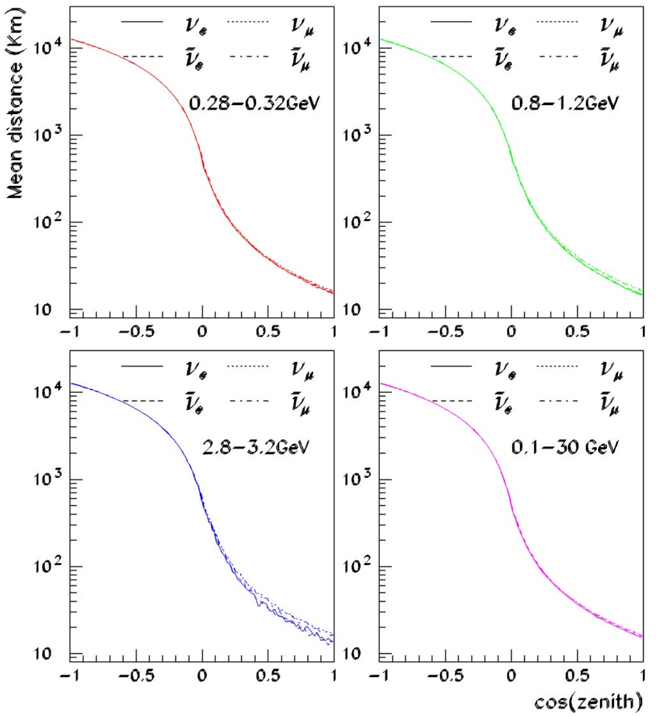

FIG. 20. Mean flying distance versus the zenithal angle distribution of ν_e, $\overline{\nu_e}$, ν_μ, and $\overline{\nu_\mu}$, in the indicated energy bins (GeV), averaged over the whole detection sphere.

are so small in comparison with the Earth diameter that it can be negligible.

J. 3-dimensional effects

The normalized distributions of angles between the directions of the incident CRs at the first collision and of the neutrinos in the end of the reaction chain, averaged over the whole detection sphere and 4π solid angle, are plotted in Fig. 21 for three energy bins.

The mean values corresponding to the different energy bins are listed in Table VI. These values indicate that the 3-dimensional effects are not important for GeV neutrinos, which is consistent with the general expectation and the result reported in [26].

The mean angles between the momenta of (1) the incident CR proton (at the first collision) and the pion-producing secondary proton (at the nth collision in the cascade), (2) the incident proton (called the pion parent) and the produced pion in the production collision (production angle), and (3) the muon parent (π or K) and the produced muon are given in Tables VII and VIII for different neutrino energy bins. From these numbers it appears that large deviations of the particle directions occur at the pion production level and only at low energy.

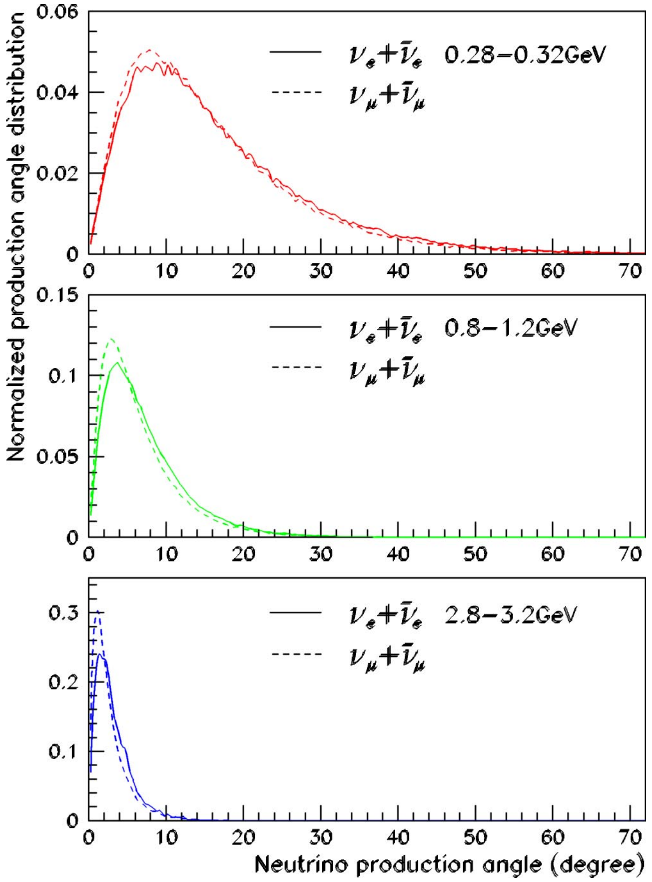

FIG. 21. Normalized distributions of neutrino production angle relative to the direction of the incident CR proton at the first collision, for three neutrino energy bins (GeV): 0.28–0.32, 0.8–1.2, 2.8–3.2.

The deflection of the charged particles by the geomagnetic field has also been examined. The largest deflection is undergone by the primary proton between the generation point and the first collision point (which depends on the generation radius). The pion deflection angle is negligible on account of its short lifetime, while for muons it is less than 4°.

Hence, it is confirmed that the 1-dimensional approximation used for GeV neutrinos in the previous calculations and simulations [5,8,9,11,12] was an acceptable approximation.

TABLE VII. Mean angles between muons, pions, and their parent particle (p,n,K) and between the parent particle and the incident CR for different energy bins of $\nu_e(\overline{\nu_e})$ (deg).

$E_{\nu_e(\overline{\nu_e})}$ (GeV)	0.1–0.2	0.28–0.32	0.8–1.2	2.8–3.2	8.0–12	20–30	0.1–30
$\langle \theta_{CR-\pi^\pm par} \rangle$	4.98	2.90	1.22	0.57	0.32	0.26	3.56
$\langle \theta_{\pi^\pm par-\pi^\pm} \rangle$	24.28	14.09	5.88	2.33	0.85	0.40	17.28
$\langle \overline{\theta}_{\mu^\pm par-\mu^\pm} \rangle$	3.73	1.95	0.72	0.30	0.26	0.25	2.55

TABLE VIII. Same as Table VII for different energy bins of $\nu_\mu(\overline{\nu_\mu})$.

$E_{\nu_\mu+\bar{\nu}_\mu}$ (GeV)	0.1–0.2	0.28–0.32	0.8–1.2	2.8–3.2	8.0–12	20–30	0.1–30
$\langle\theta_{CR-\pi^\pm par}\rangle$	5.33	2.91	1.18	0.54	0.30	0.26	3.89
$\langle\theta_{\pi^\pm par-\pi^\pm}\rangle$	23.96	13.41	5.36	1.99	0.66	0.32	16.48
$\langle\theta_{\mu^\pm par-\mu^\pm}\rangle$	4.00	2.12	0.79	0.30	0.26	0.25	2.73

V. NEUTRINO FLUX AROUND THE SUPER-KAMIOKANDE DETECTOR

In this section, the features of the atmospheric neutrino flux at the geographical position of the Super-Kamiokande (SuperK) detector are investigated. The detection sphere was defined at 0.372 km altitude, and within $(36°25'33''\pm7.5°)N$ and $(137°18'37''\pm15°)E$ latitude and longitude bins respectively.

A. Flux and flavor ratio

The calculated energy distributions of the atmospheric neutrino flux and the $\nu/\overline{\nu}$ flux ratios around the SuperK detector, averaged over 4π solid angle, are compared with the results of Honda *et al.* [9,11] in Fig. 22, for the various flavors. The flux obtained in the present work appear to be significantly smaller than in the 1-dimensional calculations for low neutrino energies.

The values of the simulated 0.1–20 GeV neutrino flux for the location of the Super-Kamiokande experiment are tabulated in Table IX. These spectra can be fit by means of the function form

$$f(E_\nu)=c_1[1.0+c_2\exp(-c_3E_\nu)]E_\nu^{c_4} \tag{1}$$

very nicely, where $f(E_\nu)$ is the flux, E_ν the neutrino energy, and c_1, c_2, c_3, and c_4 are fitting parameters given in Table X.

The functional form is inspired from [46], carrying some features of the hadroproduction of pions and kaons.

For the flavor ratios, our $(\nu_\mu+\overline{\nu_\mu})/(\nu_e+\overline{\nu_e})$ is similar to that reported in [9,11], but $\nu_e/\overline{\nu_e}$ differ evidently from all the previous 1-dimensional calculations summarized in Fig. 12 of [11].

From Figs. 1 and 4, it can be observed that the positive muon flux is overestimated in our simulation, which subse-

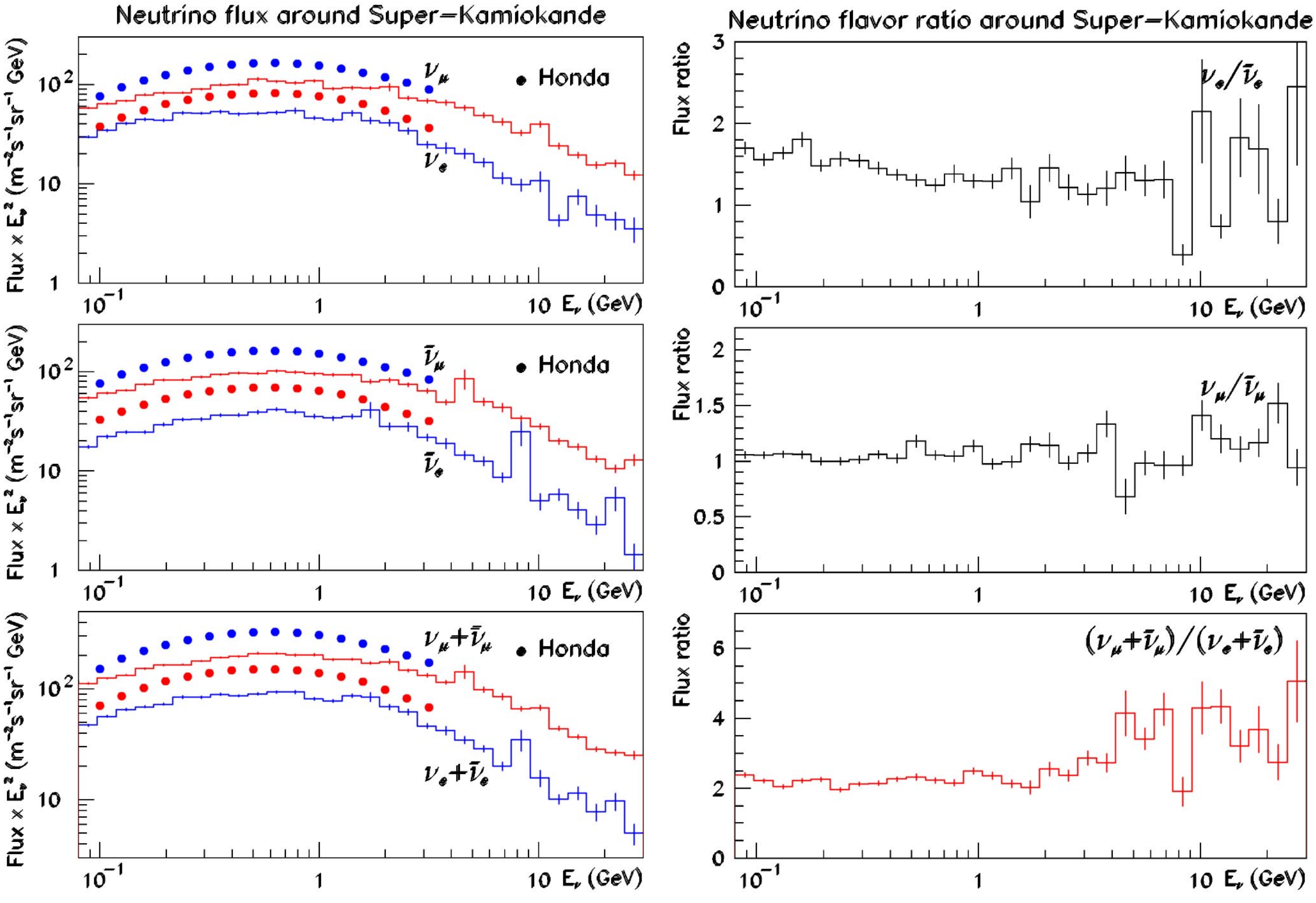

FIG. 22. Simulated atmospheric neutrino spectra and flavor ratio around Super-Kamiokande detector.

TABLE IX. Neutrino flux calculated for Super-Kamiokande experiment location.

E_ν (GeV)	Flux ($\mathrm{m^{-2} \cdot s^{-1} \cdot sr^{-1} \cdot GeV^{-1}}$)			
	ν_e	$\overline{\nu_e}$	ν_μ	$\overline{\nu_\mu}$
0.100–0.124	2948 ± 84	1780 ± 59	5229 ± 103	4915 ± 99
0.124–0.153	2078 ± 53	1324 ± 45	3677 ± 68	3629 ± 80
0.153–0.189	1595 ± 50	892 ± 29	2771 ± 63	2569 ± 48
0.189–0.233	1023 ± 30	702 ± 29	1875 ± 40	1853 ± 40
0.233–0.289	774 ± 28	485 ± 19	1260 ± 27	1266 ± 27
0.289–0.357	503 ± 15	335 ± 10	909 ± 20	901 ± 21
0.357–0.441	325 ± 12	238 ± 8	649 ± 17	610 ± 14
0.441–0.545	218 ± 8	162 ± 7	450 ± 15	389 ± 9
0.545–0.674	140 ± 5	113 ± 5	291 ± 9	268 ± 7
0.674–0.833	99 ± 6	70 ± 3	185 ± 5	183 ± 5
0.833–1.029	54 ± 2	42 ± 2	125 ± 5	114 ± 4
1.029–1.272	33 ± 1	26 ± 1	72 ± 2	70 ± 2
1.272–1.572	27 ± 2	18 ± 1	46 ± 2	46 ± 2
1.572–1.943	13.1 ± 0.8	13 ± 2	29 ± 1	26 ± 1
1.943–2.402	8.8 ± 0.6	5.7 ± 0.5	20 ± 2	17.4 ± 0.8
2.402–2.969	4.1 ± 0.3	3.9 ± 0.4	9.7 ± 0.4	10.1 ± 0.4
2.969–3.670	2.4 ± 0.2	1.8 ± 0.2	6.4 ± 0.4	5.5 ± 0.3
3.670–4.537	1.2 ± 0.2	1.1 ± 0.1	3.8 ± 0.2	3.1 ± 0.2
4.537–5.608	0.79 ± 0.08	0.54 ± 0.05	2.2 ± 0.1	3.1 ± 0.7
5.608–6.931	0.35 ± 0.04	0.27 ± 0.03	1.14 ± 0.07	1.2 ± 0.1
6.931–8.568	0.19 ± 0.02	0.19 ± 0.04	0.55 ± 0.04	0.72 ± 0.06
8.568–10.59	0.12 ± 0.03	0.22 ± 0.07	0.47 ± 0.03	0.32 ± 0.02
10.59–13.09	0.033 ± 0.005	0.036 ± 0.005	0.17 ± 0.01	0.158 ± 0.009
13.09–16.18	0.035 ± 0.006	0.022 ± 0.004	0.103 ± 0.007	0.086 ± 0.007
16.18–20.00	0.013 ± 0.003	0.009 ± 0.002	0.046 ± 0.004	0.040 ± 0.003

quently raises the $\nu_e/\overline{\nu_e}$ ratio. This observation can explain partially the large difference observed.

However, as explained at the end of Sec. IV A, it is believed that the tendency of decreasing $\nu_e/\overline{\nu_e}$ with the increasing energy should be expected because of the constraint on the $\pi^+/\pi^-(K^+/K^-)$ ratio imposed by the relevant data.

B. Zenith angle distribution

The zenith angle distribution of the flux and of the flavor ratios are shown in Fig. 23, where the enhancement of the flux in horizontal directions discussed in Sec. IV E is observed, in qualitative agreement with [24]. In the low energy bin, the maximum of this enhancement is about twice the downward- or upward-going flux out of the horizontal plane in the low energy bin. Again, it can be seen in the figure (right panel) that the flavor ratio $(\nu_\mu+\overline{\nu_\mu})/(\nu_e+\overline{\nu_e})$ also depends on the zenith angle, especially for high energy neutrinos, for the same reason as given previously.

TABLE X. Parameters used to fit the simulated neutrino spectra around the Super-Kamiokande detector.

Particle	c_1	c_2	c_3	c_4
ν_e	89.92	−1.043	0.776	−2.99
$\overline{\nu_e}$	60.47	−1.056	0.935	−2.88
ν_μ	198.4	−1.029	0.744	−2.82
$\overline{\nu_\mu}$	201.3	−1.031	0.674	−2.88

C. Azimuthal angle distribution

The azimuth angle distribution of the flux and of the flavor ratios are shown in Fig. 24 for the four neutrino species. The large angular binning used in the figure was dictated by the low counting statistics obtained, even for very long computer time used for running the simulation program. The east-west effect discussed previously in Sec. IV F is clearly observed here, more prominent for low energy neutrinos. The EW asymmetry discussed below has been estimated on the basis of these distributions.

D. Estimate of the east-west asymmetry

In addition to the atmospheric muon flux, the EW asymmetry measurements provide an important global test of the reliability of the overall approach. Since muons are charged particles, having finite lifetime, and losing energy during their flying in the atmosphere, while neutrinos have none of these features, these differences make the relation between muon and neutrino flux a complicated issue [13]. However,

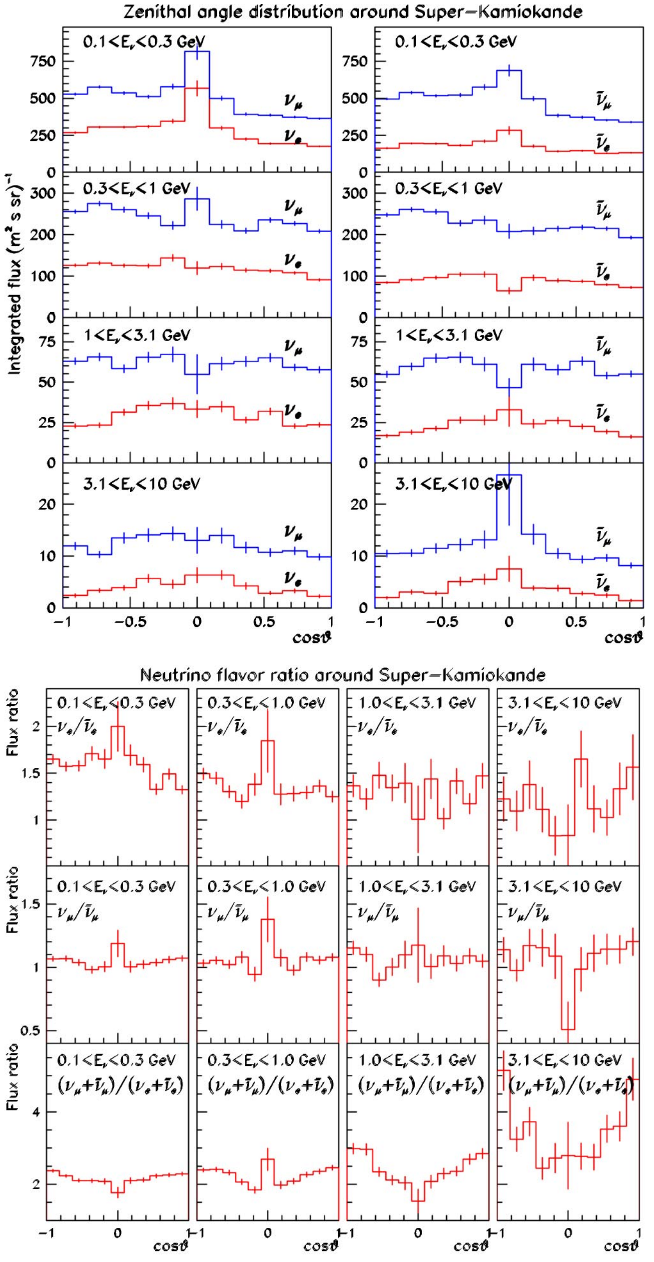

FIG. 23. Zenith angle distribution of the calculated neutrino flux and of the corresponding flavor ratios around the Super-Kamiokande detector.

the EW asymmetry is independent of physics beyond the standard model and is not expected to depend on the neutrino mass or oscillations. A reliable simulation should thus be able to reproduce the experimental EW asymmetry data quantitatively.

For the asymmetry parameter A_{EW} defined as

$$A_{EW}=\frac{N_E-N_W}{N_E+N_W},$$

N_E (N_W) being the number of eastward (westward) lepton events, the SuperK Collaboration reported the following measured values:

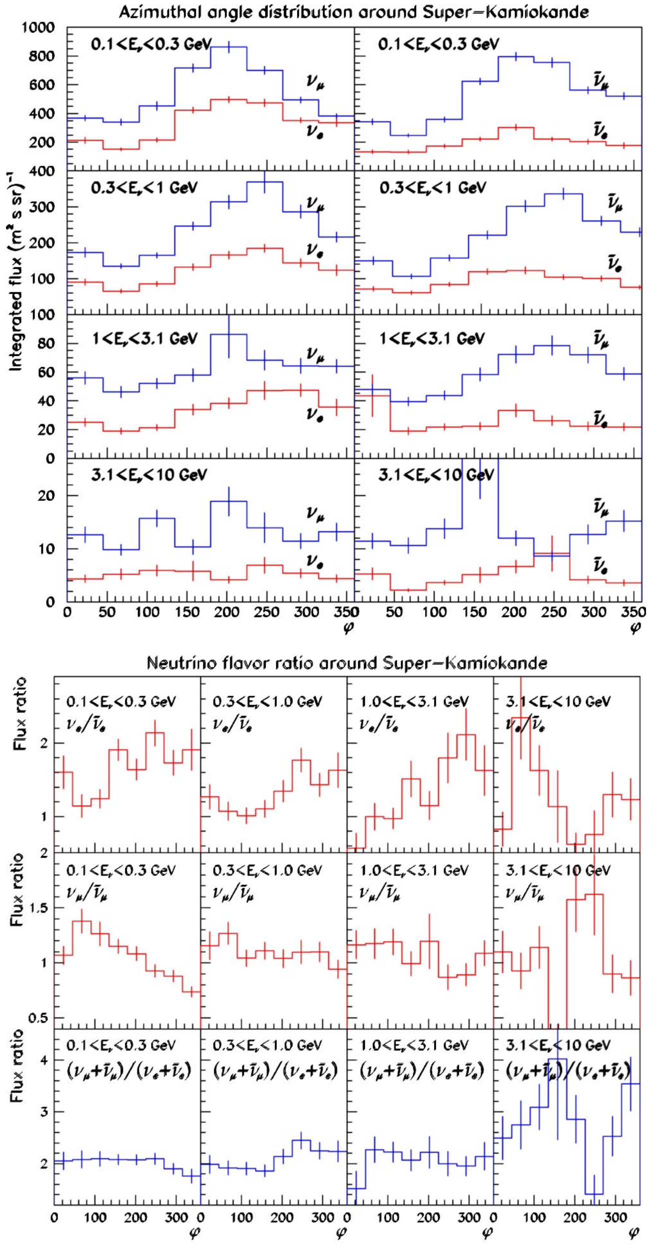

FIG. 24. Simulated azimuth angle distribution of the neutrino flux and of the flavor ratios around the SuperK detector.

$$A_{EW}^{e\text{-}like}=0.21\pm0.04, \quad A_{EW}^{\mu\text{-}like}=0.08\pm0.04,$$

for e-like and μ-like events, respectively, for a selection of single-ring events with momentum between 0.4–3 GeV and $-0.5\leqslant\cos\tau_{zenith}\leqslant0.5$, with τ_{zenith} being the zenith angle.

In order to obtain the A_{EW} value precisely, the 3-dimension differential neutrino reaction cross section [58,59] needs to be known. The asymmetry A_{EW} however could be estimated by using the following procedures.

(1) Evaluate the energy of the neutrinos which can induce lepton events over the same range as selected by Super-K, i.e., 0.4–3 GeV. The leptons with momentum p_l $\sim$100 MeV/c appear to carry 65% of the incident neutrino energy; this proportion increases to $\sim$85% for p_l

TABLE XI. Neutrino flux calculated for the SOUDAN experiment location.

E_ν (GeV)	Flux ($\mathrm{m}^{-2}\cdot\mathrm{s}^{-1}\cdot\mathrm{sr}^{-1}\cdot\mathrm{GeV}^{-1}$)			
	ν_e	$\bar{\nu}_e$	ν_μ	$\bar{\nu}_\mu$
0.100–0.124	6222 ± 240	3344 ± 163	10967 ± 313	9453 ± 257
0.124–0.153	4338 ± 175	2283 ± 97	7154 ± 194	6604 ± 188
0.153–0.189	2698 ± 100	1674 ± 83	5078 ± 159	4872 ± 154
0.189–0.233	1738 ± 71	997 ± 49	3344 ± 110	3254 ± 110
0.233–0.289	1200 ± 47	860 ± 62	2062 ± 60	2124 ± 78
0.289–0.357	771 ± 32	623 ± 45	1396 ± 53	1397 ± 52
0.357–0.441	488 ± 26	361 ± 19	936 ± 32	876 ± 36
0.441–0.545	333 ± 20	214 ± 13	628 ± 28	595 ± 31
0.545–0.674	212 ± 15	163 ± 21	359 ± 15	352 ± 15
0.674–0.833	122 ± 9	92 ± 7	231 ± 10	234 ± 12
0.833–1.029	73 ± 6	60 ± 4	145 ± 6	138 ± 7
1.029–1.272	48 ± 3	34 ± 3	80 ± 4	92 ± 6
1.272–1.572	28 ± 3	19 ± 2	52 ± 3	49 ± 3
1.572–1.943	13 ± 1	10 ± 2	30 ± 2	32 ± 4
1.943–2.402	9 ± 1	6.1 ± 0.7	19 ± 1	17 ± 1
2.402–2.969	4.4 ± 0.5	3.5 ± 0.5	9.9 ± 0.7	11.1 ± 0.9
2.969–3.670	3.4 ± 0.5	1.5 ± 0.2	5.5 ± 0.5	6.4 ± 0.6
3.670–4.537	1.6 ± 0.3	0.9 ± 0.1	3.6 ± 0.3	3.3 ± 0.4
4.537–5.608	0.53 ± 0.08	0.49 ± 0.08	2.0 ± 0.2	1.5 ± 0.2
5.608–6.931	0.44 ± 0.07	0.43 ± 0.09	1.1 ± 0.1	0.9 ± 0.1
6.931–8.568	0.16 ± 0.03	0.12 ± 0.02	0.58 ± 0.05	0.6 ± 0.1
8.568–10.59	0.10 ± 0.02	0.08 ± 0.02	0.32 ± 0.03	0.29 ± 0.03
10.59–13.09	0.031 ± 0.007	0.04 ± 0.01	0.20 ± 0.02	0.16 ± 0.02
13.09–16.18	0.017 ± 0.004	0.012 ± 0.004	0.10 ± 0.01	0.09 ± 0.01
16.18–20.00	0.016 ± 0.005	0.022 ± 0.009	0.053 ± 0.006	0.037 ± 0.005

$=1$ GeV/c [1]. It can be assumed that the fraction keeps on increasing and asymptotically tends to 100%. Based on this supposition, the corresponding neutrino energies of about 0.55 and 3.1 GeV associated with the 0.4 and 3 GeV lepton events are obtained respectively.

(2) Estimate the production angle of the neutrino induced lepton. This can be done following [21], by noting that the interested neutrino energy range is above 0.5 GeV within which there is no large difference between the production angles of ν_e and ν_μ events. Another way is by using the values 55° at $p_l=0.4$ GeV/c and 20° at $p_l=1.5$ GeV/c as reported in [1], and fit them as a function of the neutrino energy, assuming that the angle smoothly tends to zero as expected from basic kinematics.

(3) For each neutrino with energy between 0.55 and 3.1 GeV, lepton events are randomly generated with the scattering angle relative to the neutrino direction estimated as above and with a uniform distribution for the azimuth angle. After weighting by the energy-dependent cross section [28,60,61] and application of a normalization procedure, the events with $|\cos(\theta_l)|\leqslant 0.5$ are selected to calculate the asymmetry parameter.

Using the above procedure, the following values are obtained for the EW asymmetry parameters for e-like and μ-like events around the Super-Kamiokande detector:

$$A^{e\text{-}like}_{E\text{-}W}=0.12\pm0.03,\qquad A^{\mu\text{-}like}_{E\text{-}W}=0.13\pm0.02.$$

In contrast, the EW asymmetries obtained for the two-neutrino flux with the same cut over the zenithal angle and within the same energy bin of [0.55,3.1] GeV are

$$A^{\nu_e+\bar{\nu}_e}_{E\text{-}W}=0.17\pm0.03,\qquad A^{\nu_\mu+\bar{\nu}_\mu}_{E\text{-}W}=0.22\pm0.02,$$

which shows that the predicted neutrino asymmetry is largely washed out by the angular distribution of the neutrino induced lepton production process.

The larger EW flux asymmetry obtained for $\nu_\mu(\bar{\nu}_\mu)$ than for $\nu_e(\bar{\nu}_e)$ can be qualitatively understood: The production of $\nu_e(\bar{\nu}_e)$ takes place in the second step of the pion decay

TABLE XII. Fitting parameters for simulated neutrino spectra around the SOUDAN detector.

Particle	c_1	c_2	c_3	c_4
ν_e	105.0	−1.034	0.869	−3.12
$\bar{\nu}_e$	63.9	−1.069	1.235	−2.99
ν_μ	143.0	−0.970	1.859	−2.67
$\bar{\nu}_\mu$	362.2	−1.021	0.416	−3.16

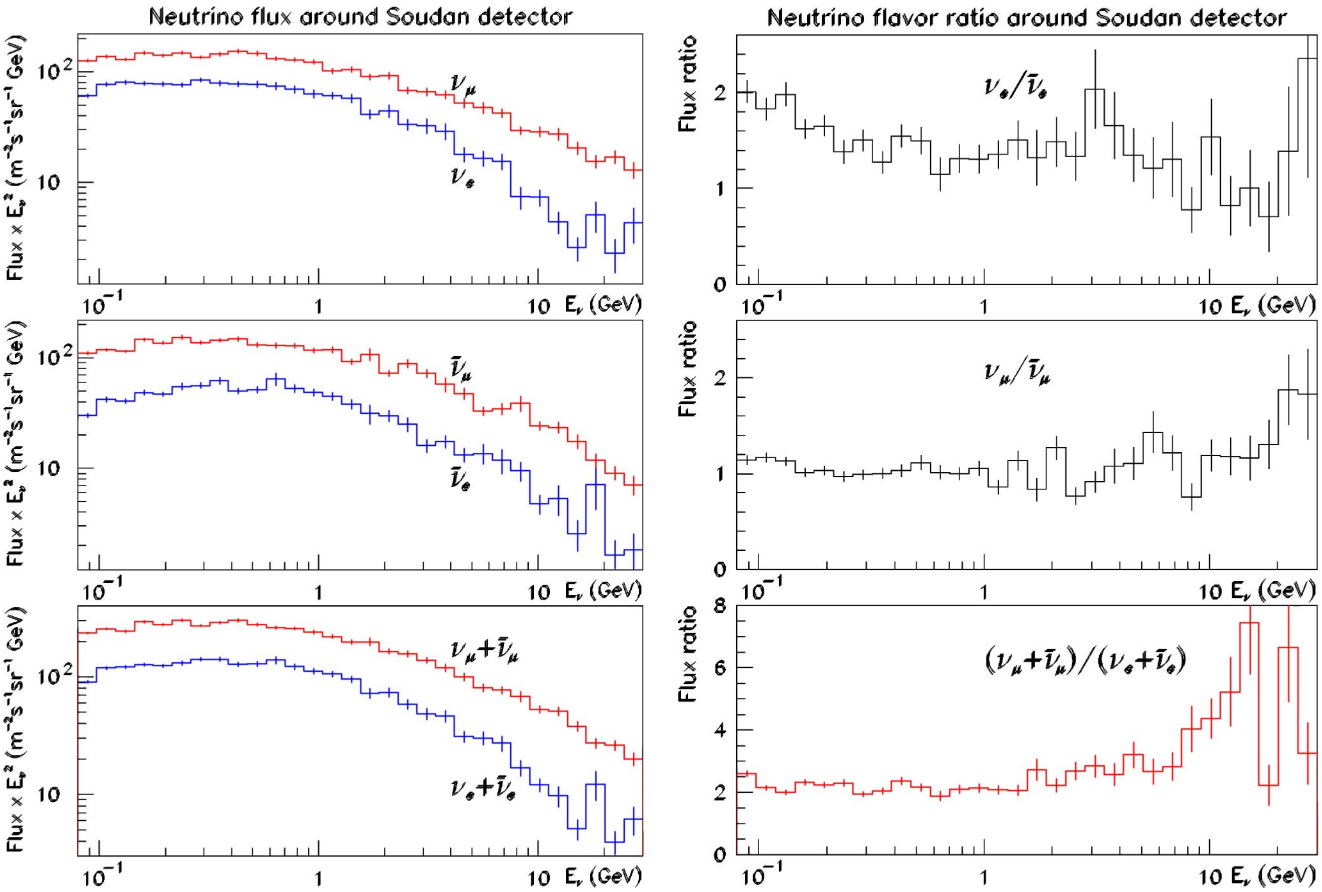

FIG. 25. Simulated atmospheric neutrino spectra and flavor ratios around the SOUDAN detector.

chain. The decay kinematics should thus wash out the EW asymmetry of electron neutrinos more than for muon neutrinos which are produced dominantly in the first stage of the decay sequence.

In comparison with the data [20] and other simulation results [21], the present calculations depart further from the data. It can be noted that the present overestimated ratio of π^+/π^- may affect this prediction. More work is still needed to clear up this problem.

VI. NEUTRINO FLUX AROUND THE SOUDAN EXPERIMENT

The same calculations for the simulated atmospheric neutrino flux around the SOUDAN detector as for the Super-K experiment in the previous section are reported in this section. The normalization area used in the calculations corresponds to the geographical latitude and longitude bin of $(48° \pm 5°)$N and $(98° \pm 10°)$W, respectively. The altitude is taken the same as for Super-K, as we have seen from Fig. 17, the error resulting from the altitude difference between Super-Kamiokande and SOUDAN detector should be negligible in evaluating the flux and relevant distributions.

A. Flux and flavor ratio

The energy spectra and energy dependence of flavor ratios, averaged over a 4π solid angle, are shown in Fig. 25. Due to the relatively high geomagnetic latitude of the SOUDAN detector location, and hence to the lower geomagnetic cutoff, the calculated neutrino flux are much higher than found for Super-K.

Also, the 0.1–20.0 GeV neutrino energy spectra simulated for the SOUDAN experiment site are tabulated in Table XI. They can be fit with the same functional form [relation (1)]. The coefficients are listed in Table XII.

B. Zenith angle distributions

The calculated zenithal angle distributions are shown in Fig. 26, for the same energy bins as previously, where the high geomagnetic latitude feature of such a distribution illustrated in Sec. IV E is evident.

C. Azimuth angle distributions

Figure 27 shows the azimuth angle distributions of the atmospheric neutrino flux around the SOUDAN detector, based on which the EW asymmetry parameter for neutrino flux and lepton events in the detector are also estimated along the same lines as for the Super-K experiment.

The EW asymmetry for the lepton events is predicted as

$$A_{E\text{-}W}^{e\text{-}like} = 0.006 \pm 0.037, \quad A_{E\text{-}W}^{\mu\text{-}like} = 0.026 \pm 0.024,$$

while for the neutrino flux the following values are obtained:

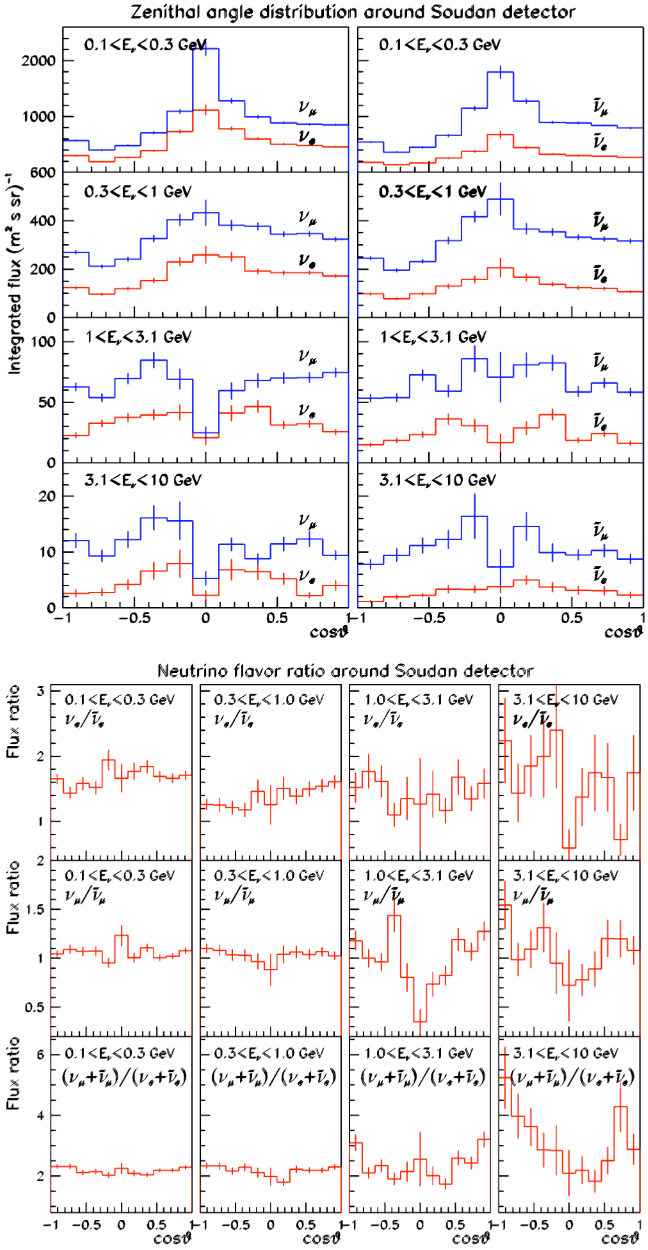

FIG. 26. Zenith angle distributions of the simulated neutrino flux and flavor ratios around the SOUDAN detector.

$$A_{E\text{-}W}^{\nu_e+\overline{\nu}_e}=0.068\pm0.043,\qquad A_{E\text{-}W}^{\nu_\mu+\overline{\nu}_\mu}=0.071\pm0.025,$$

with the same selection criteria as used for Super-K in the previous section. It would therefore be of great interest to have some experimental values for this experiment to provide a further test the present approach and a step forward to a better global understanding of the problem.

VII. CONCLUSION AND DISCUSSION

In summary, the atmospheric neutrino flux has been simulated by means of an event generator dedicated to the general cosmic ray–atmosphere interactions, developed to account for the AMS01 results, originally. The successful calculations reported previously on the hadron and lepton flux close to Earth strongly support the method and the models used.

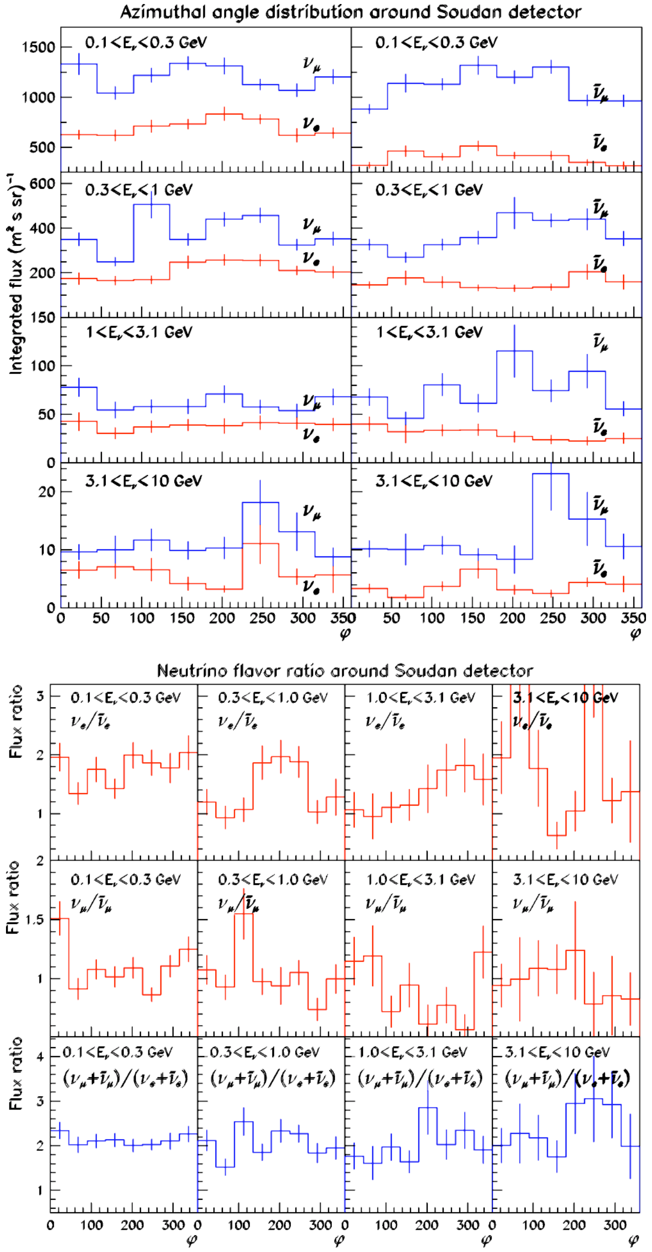

FIG. 27. Azimuth angle distributions of the simulated neutrino flux and of the flavor ratios around the SOUDAN detector.

In this work, the CAPRICE and HEAT muon flux data measured at various altitudes in the atmosphere, from about sea level to 38 km, have been successfully reproduced, providing further grounds to the correctness of the approach.

A significantly lower absolute value of the flux than found in 1-dimensional calculations [9,11] in the low energy range has been reported here. Also, the $\nu_e/\overline{\nu}_e$ ratio is largely different from all the previous calculations. In addition, the present results are in agreement with similar results reported in [23].

Detailed features of the neutrino flux—zenithal and azimuthal angle distribution and flavor ratios at different latitudes, corresponding energy distributions, production altitude, and production angle distributions—have been calculated and discussed. The components originating from cosmic rays and from the atmospheric cascade have been distinguished and discussed separately. All the observed features of the calculated flux could be traced back to the primary spectra, $\pi^+/\pi^-(K^+/K^-)$ ratio, muon kinetics, geomagnetic effect, and geometry.

Specific 3-dimensional effects seen in the simulation results are very small, which indicates that the 1-dimensional approximation provides reliable results for GeV neutrino flux calculations.

The calculations fail to reproduce quantitatively the east-west asymmetry of the atmospheric neutrino-induced events in the Super-K detector. More investigations are needed to understand this disagreement.

A complete comparison of the parametrizations used to describe the various hadronic production channels with the available data will be reported in detail later.

ACKNOWLEDGMENTS

The authors are grateful to N. Mokhov and V. Naumov for helpful discussion during the course of this work and to M. Boezio, M. Circella, and T. Sanuki for making their data available and for providing experimental details.

[1] Super-Kamiokande Collaboration, Y. Fukuda *et al.*, Phys. Rev. Lett. **81**, 1562 (1998); Phys. Lett. B **433**, 9 (1998); **436**, 33 (1998).

[2] Soudan 2 Collaboration, W. W. M. Allison *et al.*, Phys. Lett. B **449**, 137 (1999); W. W. M. Allison *et al.*, *ibid.* **391**, 491 (1997).

[3] W. Frati, T. K. Gaisser, A. K. Mann, and T. Stanev, Phys. Rev. D **48**, 1140 (1993).

[4] G. L. Fogli, E. Lisi, A. Marrone, and G. Scioscia, Phys. Rev. D **59**, 033001 (1998).

[5] E. V. Bugaev and V. A. Naumov, Phys. Lett. B **232**, 391 (1989).

[6] P. Lipari, Astropart. Phys. **1**, 195 (1993).

[7] D. H. Perkins, Astropart. Phys. **2**, 249 (1994).

[8] G. Barr, T. K. Gaisser, and T. Stanev, Phys. Rev. D **39**, 3532 (1989); V. Agrawal, T. K. Gaisser, P. Lipari, and T. Stanev, *ibid.* **53**, 1314 (1996).

[9] M. Honda, K. Kasahara, K. Hikada, and S. Midorikawa, Phys. Lett. B **248**, 193 (1990).

[10] L. V. Volkova, Yad. Fiz. **31**, 1510 (1980) [Sov. J. Nucl. Phys. **31**, 784 (1980)].

[11] M. Honda, T. Kajita, K. Kasahara, and S. Midorikawa, Phys. Rev. D **52**, 4985 (1995).

[12] H. Lee and Y. S. Koh, Nuovo Cimento Soc. Ital. Fis., B **105**, 883 (1990).

[13] T. K. Gaisser, Nucl. Phys. B (Proc. Suppl.) **87**, 145 (2000).

[14] R. Engel, T. K. Gaisser, and T. Stanev, Phys. Lett. B **472**, 113 (2000).

[15] T. K. Gaisser *et al.*, Phys. Rev. D **54**, 5578 (1996).

[16] AMS Collaboration, J. Alcaraz *et al.*, Phys. Lett. B **472**, 215 (2000); **484**, 10 (2000).

[17] BESS Collaboration, T. Sanuki *et al.*, Astrophys. J. **545**, 1135 (2000).

[18] M. Honda *et al.*, in Proceedings of 27th ICRC, 2001, Hamburg, p. 1162.

[19] N. V. Mokhov and S. I. Striganov, Workshop on the Front End of a Muon Collider, 1998, pp. 453–459.

[20] Super-Kamiokande Collaboration, T. Futagami *et al.*, Phys. Rev. Lett. **82**, 5194 (1999).

[21] T. Kajita and Y. Totsuka, Rev. Mod. Phys. **73**, 85 (2001).

[22] M. Honda, T. Kajita, K. Kasahara, and S. Midorikawa, Phys. Rev. D **64**, 053011 (2001).

[23] G. Fiorentini, V. A. Naumov, and F. L. Villante, Phys. Lett. B **510**, 173 (2001); G. Fiorentini, V. A. Naumov, and F. L. Villante, hep-ph/0106014; in Proceedings of 27th ICRC, Hamburg, 2001.

[24] P. Lipari, Astropart. Phys. **14**, 153 (2000); **14**, 171 (2000).

[25] T. K. Gaisser, Astropart. Phys. **16**, 285 (2002).

[26] G. Battistoni *et al.*, Astropart. Phys. **12**, 315 (2000); G. Battistoni, A. Ferrari, T. Montaruli, and P. R. Sala, in Proceedings of 27th ICRC, Hamburg, 2001; G. Battistoni *et al.*, hep-ph/0207035.

[27] Y. Tserkovnyak, R. Komar, C. Nally, and C. Waltham, in Proceedings of 27th ICRC, Hamburg, 2001, hep-ph/9907450.

[28] V. Plyaskin, Phys. Lett. B **516**, 213 (2001).

[29] Yong Liu, L. Derome, and M. Buénerd, in Proceedings of 27th ICRC, Hamburg, 2001.

[30] J. Wentz *et al.*, in Proceedings of 27th ICRC, Hamburg, 2001.

[31] HEAT Collaboration, S. Coutu *et al.*, Phys. Rev. D **62**, 032001 (2000).

[32] CAPRICE Collaboration, J. Kremer *et al.*, Phys. Rev. Lett. **83**, 4241 (1999); M. Boezio *et al.*, *ibid.* **82**, 4757 (1999).

[33] MASS Collaboration, R. Bellotti *et al.*, Phys. Rev. D **60**, 052002 (1999).

[34] AMS Collaboration, J. Alcaraz *et al.*, Phys. Lett. B **494**, 193 (2000).

[35] L. Derome *et al.*, Phys. Lett. B **489**, 1 (2000); L. Derome and M. Buénerd, Nucl. Phys. **A688**, 66c (2001).

[36] L. Derome, M. Buénerd, and Yong Liu, Phys. Lett. B **515**, 1 (2001).

[37] L. Derome and M. Buénerd, Phys. Lett. B **521**, 139 (2001); see also Proceedings of ICRC 2001, Hamburg, 2001.

[38] C. Y. Huang, L. Derome, and M. Buénerd (in preparation).

[39] M. S. Vallarta, in *Handbuch der Physik*, edited by S. Flügge (Springer-Verlag, Berlin, 1961).

[40] J. S. Perko, Astron. Astrophys. **184**, 119 (1984); see M. S. Potgieter, in Proceedings of ICRC, Calgary, 1993, p. 213, for a recent review of the subject.

[41] J. A. Simpson, Ann. Rev. Nucl. Sci. **33**, 323 (1983).

[42] B. Wiebel-Sooth, P. L. Biermann, and H. Meyer, Astron. Astrophys. **330**, 389 (1998).

[43] G. N. Agakishiev *et al.*, Sov. J. Nucl. Phys. **33**, 552 (1981).

[44] G. N. Agakishiev *et al.*, Sov. J. Nucl. Phys. **40**, 767 (1984); SKM-200 Collaboration, A. Kh. Abdurakhimov *et al.*, Nucl.

Phys. **A362**, 376 (1981); G. N. Agakishiev *et al.*, Z. Phys. C **27**, 177 (1985); R. N. Bekmirzaev, E. N. Kladnitskaya, and S. A. Sharipova, Yad. Fiz. **58**, 1 (1995) [Phys. At. Nucl. **58**, 58 (1995)].

[45] A. E. Hedin, J. Geophys. Res. **96**, 1159 (1991).

[46] A. N. Kalinovsky, N. V. Mokhov, and Y. P. Nikitin, in *Passage of High Energy Particles Through Matter* (AIP, New York, 1989).

[47] Yong Liu, L. Derome, and M. Buénerd, ''Parametrization for the Inclusive Production Cross Section of proton induced $\pi^{\pm}$ particles on nuclei,'' ISN Internal Report No. 01-012, 2001.

[48] Particle Data Group, D. E. Groom *et al.*, Eur. Phys. J. C **15**, 1 (2000).

[49] S. Hayakawa, Phys. Rev. **108**, 1533 (1957); G. Barr, T. K. Gaisser, and T. Stanev, Phys. Rev. D **39**, 3532 (1989).

[50] L. Derome, Yong Liu, and M. Buénerd, in Proceedings of ICRC 2001, Hamburg, 2001, OG1.018.

[51] P. Hansen, for The WIZARD/CAPRICE Collaboration, in Proceedings of 27th ICRC, Hamburg, 2001.

[52] BESS Collaboration, T. Sanuki *et al.*, Phys. Lett. B **541**, 234 (2002); M. Motoki *et al.*, astro-ph/0205344.

[53] D. R. F. Cochran *et al.*, Phys. Rev. D **6**, 3085 (1972).

[54] H. Boggild *et al.*, Phys. Rev. C **59**, 328 (1999).

[55] D. Antreasyan *et al.*, Phys. Rev. D **19**, 764 (1979); S. Fredriksson, *ibid.* **18**, 4144 (1978).

[56] T. K. Gaisser and T. Stanev, Phys. Rev. D **57**, 1977 (1998).

[57] T. K. Gaisser and M. Honda, hep-ph/0203272.

[58] P. Lipari, M. Lusignoli, and F. Sartogo, Phys. Rev. Lett. **74**, 4384 (1995); E. A. Paschos and J. Y. Yu, Phys. Rev. D **65**, 033002 (2002).

[59] Kamiokande Collaboration, M. Nakahata *et al.*, J. Phys. Soc. Jpn. **55**, 3786 (1986).

[60] O. Erriquez *et al.*, Phys. Lett. **80B**, 309 (1979).

[61] Particle Data Group, K. Hikasa *et al.*, Phys. Rev. D **45**, S1 (1992), p. 82, and references therein.